

Analytical and numerical studies of the structure of steady separated flows

By ODUS R. BURGGRAF

Department of Aeronautical and Astronautical Engineering,
The Ohio State University, Columbus, Ohio

(Received 7 July 1964 and in revised form 21 June 1965)

The viscous structure of a separated eddy is investigated for two cases of simplified geometry. In § 1, an analytical solution, based on a linearized model, is obtained for an eddy bounded by a circular streamline. This solution reveals the flow development from a completely viscous eddy at low Reynolds number to an inviscid rotational core at high Reynolds number, in the manner envisaged by Batchelor. Quantitatively, the solution shows that a significant inviscid core exists for a Reynolds number greater than 100. At low Reynolds number the vortex centre shifts in the direction of the boundary velocity until the inviscid core develops; at large Reynolds number, the inviscid vortex core is symmetric about the centre of the circle, except for the effect of the boundary-layer displacement-thickness. Special results are obtained for velocity profiles, skin-friction distribution, and total power dissipation in the eddy. In addition, results of the method of inner and outer expansions are compared with the complete solution, indicating that expansions of this type give valid results for separated eddies at Reynolds numbers greater than about 25 to 50. The validity of the linear analysis as a description of separated eddies is confirmed to a surprising degree by numerical solutions of the full Navier–Stokes equations for an eddy in a square cavity driven by a moving boundary at the top. These solutions were carried out by a relaxation procedure on a high-speed digital computer, and are described in § 2. Results are presented for Reynolds numbers from 0 to 400 in the form of contour plots of stream function, vorticity, and total pressure. At the higher values of Reynolds number, an inviscid core develops, but secondary eddies are present in the bottom corners of the square at all Reynolds numbers. Solutions of the energy equation were obtained also, and isotherms and wall heat-flux distributions are presented graphically.

Introduction

Separated flow is an old subject in the literature of fluid mechanics. For example, in his study of hydraulics in the fifteenth century, Leonardo da Vinci observed and sketched recirculating eddies formed in the flow over various configurations (Giacomelli 1934; Hoerner 1958). From his observations, he concluded that the forebody provides the dominant part of the drag of a bluff body. †

† Even at this early period, flow visualization techniques were available; da Vinci used millet seed to observe the particle paths on his water table, and pointed out that illuminated dust particles served the same purpose in air.

Isaac Newton formulated his well-known theory of drag based on the idea of particles striking only the front of a moving body. Particle reflexions of several kinds were considered, but in each case the rear of the body was completely shielded from the flow. (The successful application of one of his theories awaited the recent development of hypersonic flight.) At a later time the names of Helmholtz and Kirchhoff became associated with the subject through their elegant mathematical treatment of the problem. In spite of this long history and the famous names associated with it, the fact is that a real understanding of the subject has not yet been obtained. Many theoretical models have been proposed, but other than the complete Navier-Stokes equations, none has been accepted as a well-founded theory.






Reynolds number range	Flow configuration	Remarks
$R \ll 1$		Steady flow, no wake
$R \sim 1$		Steady flow, non-circulating wake
$R \sim 10^2$		Relatively steady, recirculating flow
$R \sim 10^3$		Stable vortex street
$R > 10^5$		Turbulent wake

TABLE 1. Flow régimes for circular cylinder

In the present study, we undertake the problem of determining the effect of Reynolds number on the structure of the flow in a steady recirculating eddy, of the kind found in the separated region behind a bluff body. To place our problem in perspective, table 1 presents the various régimes of flow experienced by a bluff body (circular cylinder) immersed in an incompressible fluid. At the lowest Reynolds numbers the flow exhibits complete fore-and-aft symmetry for a symmetric body. The appearance of a wake first occurs at a Reynolds number R of the order of 1, and the flow separates from the rear of the cylinder forming a recirculating eddy for R greater than about 5. The steady recirculating wake persists for at least a decade in Reynolds number, growing in length until oscillations in the downstream wake progress forward to the recirculating eddy. The steady flow then breaks down into the familiar Kármán vortex street for

R of the order of 100. This pattern of alternating vortices exists over approximately two decades of Reynolds number, breaking down into an irregular unsteady wake, and finally a completely turbulent wake for R greater than 10^5 . The limits on these flow régimes are not fixed, since they depend strongly on the conditions of the experiment. For example, the value $R = 40$ is conventional for the breakdown of the steady recirculating flow. However, this value probably is a lower limit of erratic experimental values for circular cylinders; far higher values have been observed. Prandtl (1934) shows a stable recirculating eddy behind an oblate elliptic cylinder at $R = 80$, and Grove, Shair, Petersen & Acrivos (1964) have stabilized the flow behind a circular cylinder to Reynolds numbers as high as 300 by use of the stabilizing effect of tunnel walls and a downstream splitter plate. Moreover, compressibility of the fluid has a strong stabilizing effect, so that steady recirculating wakes have been observed in supersonic flows for $R > 10^6$, far higher than for low-speed flows (Chapman, Kuehn & Larson 1956; Nash 1962).

The flow régimes just discussed have been established from experiments; the theory has been established only at low Reynolds numbers, and even then the calculation is not trivial. The classical theory of Stokes, in which the inertial terms are dropped from the Navier–Stokes equations, is deficient for the case of a body in an unbounded stream, in that Stokes flow cannot properly represent conditions both at the body and at infinity. This difficulty has been resolved by Kaplun and his co-workers by use of the method of inner and outer expansions. The Stokes flow is the inner expansion which is matched through an overlapping region to the Oseen expansion in the outer region about the point at infinity. This method has been applied to both the sphere and cylinder by Kaplun & Lagerstrom (1957), Kaplun (1957), and in more detail by Proudman & Pearson (1957). Van Dyke (1964) has compared the two-term expansion with both numerical and experimental results for the flow behind a sphere, and good agreement is observed for Reynolds numbers up to 70 for the shape of the standing eddy and up to $R = 120$ for the length of the eddy. This agreement is far beyond what might be expected of two terms of an expansion in small Reynolds number. The author has made a similar comparison of a two-term Stokes expansion for the Jeffery–Hamel wedge flows at $R \sim 100$. In this case agreement is good only when the wedge flow is entirely viscous, such as for the separation-type profiles exhibited by the divergent-wedge flows. From results presented later in this article, it will be seen that a recirculating eddy is completely viscous for Reynolds numbers up to 100. Even so, Van Dyke's results are remarkable in that the shape of the eddy is a free boundary, subject to distortion by the outer flow.

For higher Reynolds numbers, the flow field might be constructed in a similar way by adding higher order terms to the limiting steady flow for $R \rightarrow \infty$. Thus Imai (1960) has extended the Helmholtz–Kirchhoff free-streamline theory to finite Reynolds number by considering the flow induced by the shear layer developed along the free streamline. Unfortunately, it is not clear that the free-streamline model is the correct limit for $R \rightarrow \infty$. Alternatively, Batchelor (1956*a*) proposed as a limiting steady flow a finite wake embodying a residual recirculating eddy having uniform vorticity. This model was earlier used by Batchelor

(1954) in treating a problem in free convection. A third alternative is suggested by Grove (1963), who concludes from extrapolation of his experiments that the limiting steady wake is infinite in length, finite in width, and remains viscous in character even in the limit $R \rightarrow \infty$ (owing to its infinite length). Since three models proposed so recently are in such basic disagreement, it must be concluded that the classical wake problem is not yet resolved. On the other hand, many problems exist for which the separation region is known to be of finite extent, as within a cavity in a solid wall, or in the vicinity of the base of a body in supersonic flight. For such problems, Batchelor's model appears to be the correct steady flow in the limit $R \rightarrow \infty$.

Batchelor's model of separated eddies is based on an exact integral theorem derived from the Navier-Stokes equations for steady flow (a corresponding theorem was derived for axisymmetric flow). With the assumption that viscous effects are restricted to a thin layer along the separation streamline, the uniform vorticity result then follows from this theorem. The specific value of the vorticity is obtained by matching to the external boundary conditions, using the boundary-layer equations. Batchelor (1956*b*) illustrated the matching procedure for a circular eddy; for this case the pressure gradient terms drop out of the boundary-layer equations. Unfortunately, for a more general case the pressure terms prevent the matching process being carried out in a simple manner. Some of Batchelor's results for plane flow were given concurrently by Feynman & Lagerstrom (1956), who attribute the uniform vorticity limit to Prandtl in 1905. These authors point out that the existence of secondary eddies may invalidate the assumption of a thin viscous layer. In addition to this effect, however, the concept of secondary eddies suggests that the uniform vorticity model is not unique; that is, it is possible to construct multiple eddies, each having its own uniform vorticity, within a prescribed contour. In this case Batchelor's model would presume to describe a primary eddy, with the secondary eddies producing only a minor effect.

The purpose of the present study is threefold: (1) to determine the structure of a viscous eddy as a function of Reynolds number; (2) to test the validity of the uniform vorticity model as the limiting solution of the Navier-Stokes equations for steady flow; and (3) if valid, to determine the range of finite Reynolds numbers for which the uniform vorticity model remains a good approximation. To concentrate attention on the viscous structure of the eddy itself, the model chosen is the recirculating flow within a fixed finite cavity. Two configurations are studied. In § 1, an analytical solution is obtained for the circular cavity at all Reynolds numbers, based on a linearized model (the inviscid limit for this problem was treated by Batchelor 1956*b*). Then in § 2, numerical solutions of the full Navier-Stokes equations are presented for a square cavity, confirming the linearized treatment of the circle and, further, demonstrating the effect of pressure gradient in forming secondary eddies in the corners. In addition, thermal conditions in a recirculating eddy are considered in § 2 with results for the temperature distribution analogous to those of vorticity for the kinematic conditions

1. Linearized analysis of circular eddies

1.1. Formulation and general solution

Consider now a steady, viscous, incompressible flow recirculating within a closed circular boundary (figure 1). Although the circular shape of the boundary is fixed, the velocity on the boundary may be prescribed arbitrarily. Introduce

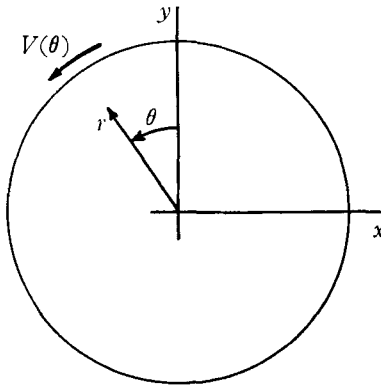


FIGURE 1. Notation for circular eddy.

non-dimensional variables $\hat{r} = r/a$, $\hat{u} = u/\Omega a$, $\hat{\psi} = \psi/\Omega a^2$, $\hat{\omega} = \omega/\Omega$ where a is the radius of the circle and Ω is a characteristic angular velocity on the boundary surface. Then in terms of the stream function $\hat{\psi}$ and the vorticity $\hat{\omega}$, the Navier–Stokes equations in cylindrical co-ordinates become

$$\nabla^2 \hat{\psi} = -\hat{\omega}, \quad \nabla^2 \hat{\omega} = \frac{R}{\hat{r}} \left[\frac{\partial \hat{\psi}}{\partial \theta} \frac{\partial \hat{\omega}}{\partial \hat{r}} - \frac{\partial \hat{\psi}}{\partial \hat{r}} \frac{\partial \hat{\omega}}{\partial \theta} \right], \tag{1.1}$$

where R is the Reynolds number $\Omega a^2/\nu$. We now formulate a linearized problem by restricting our attention to flows which are slightly perturbed from a basic flow, which we take to be solid-body rotation (a trivial solution of the Navier–Stokes equations for all Reynolds numbers). The basic flow is defined by

$$\hat{u}_\theta = \hat{r}, \quad \hat{u}_r \equiv 0, \quad \hat{\psi} = \frac{1}{2}(1 - \hat{r}^2), \quad \hat{\omega} = 2.$$

In the usual way, add a perturbation to each of the dependent variables of the basic flow, substitute into the above form of the Navier–Stokes equations, and retain only first-order terms in the perturbation quantities. The result is a linear equation for the vorticity

$$\nabla^2 \omega = R \partial \omega / \partial \theta. \tag{1.2}$$

(In this equation and the following the symbol $\hat{\ }^{\wedge}$ is understood.) This linearization procedure is quite similar to the Oseen linearization, differing in that the basic flow is a uniform rotation in this case and a uniform translation in the Oseen problem.

Solutions of (1.2) are found by separation of variables. Putting

$$\omega = f_n(r) e^{in\theta},$$

we find that f_n must satisfy a variation of Bessel’s equation

$$r^2 f_n'' + r f_n' - (n^2 + inRr^2) f_n = 0. \tag{1.3}$$

Solutions regular at the origin are the modified Bessel functions of first kind of order n . Hence, by adding the elementary solutions, the vorticity is expressed by the series

$$\omega = \omega_0 - iR \sum_1^{\infty} n b_n I_n\{r \sqrt{(inR)}\} e^{in\theta}. \quad (1.4)$$

The constant multiplier $(-inR)$ was chosen to obtain a simple form for the stream function, as follows. Putting

$$\psi = F_n(r) e^{in\theta},$$

then (1.1) gives the non-homogeneous equation

$$r^2 F_n'' + r F_n' - n^2 F_n = -r^2 f_n. \quad (1.5)$$

Comparing (1.5) with (1.3), we see that a particular solution of (1.5) is just $F_n(r) = i f_n(r)/nR$. Moreover, the homogeneous part of (1.5) has the solution $F_n = r^n$, regular at the origin. Consequently, corresponding to (1.4), the stream function is expressed by the series.

$$\psi = [a_0 - \frac{1}{4}\omega_0 r^2] + \sum_1^{\infty} [a_n r^n + b_n I_n\{r \sqrt{(inR)}\}] e^{in\theta}. \quad (1.6)$$

The leading term represents solid body rotation with angular velocity $\frac{1}{2}\omega_0$; the constants a_n and b_n in the higher-order terms† are determined from the boundary conditions on the enclosing streamline, which may be expressed in the general form

$$\left. \begin{aligned} \psi &= 0, \\ \frac{\partial \psi}{\partial r} &= -\sum_0^{\infty} A_n e^{in\theta} \end{aligned} \right\} \text{ on } r = 1. \quad (1.7)$$

Substituting the expansion for ψ , the coefficients are found to be related by

$$\left. \begin{aligned} a_0 &= \frac{1}{4}\omega_0 = \frac{1}{2}A_0, \\ a_n &= \frac{A_n}{\sqrt{(inR)}} \frac{I_n\{\sqrt{(inR)}\}}{I_{n+1}\{\sqrt{(inR)}\}}, \\ b_n &= -\frac{A_n}{\sqrt{(inR)}} \frac{1}{I_{n+1}\{\sqrt{(inR)}\}}. \end{aligned} \right\} \quad (1.8)$$

With the coefficients determined by (1.8), the solution can be evaluated for any value of Reynolds number. Before considering special cases, let us derive the asymptotic forms of the solution for both low and high Reynolds number.

1.2. The Stokes limit: $R \rightarrow 0$

From the well-known expansion of the Bessel function for small argument

$$I_n(x) = i^{-n} J_n(ix) = \frac{1}{n!} \left(\frac{x}{2}\right)^n \left[1 + \frac{1}{n+1} \left(\frac{x}{2}\right)^2 + \dots\right],$$

the following asymptotic results are obtained

$$\begin{aligned} r_n I_n\{\sqrt{(inR)}\} - I_n\{r \sqrt{(inR)}\} &\sim (1-r^2) r^n (inR)^{\frac{1}{2}(n+2)/2^{n+2}} (n+1)!, \\ \sqrt{(inR)} I_{n+1}\{\sqrt{(inR)}\} &\sim (inR)^{\frac{1}{2}(n+2)/2^{n+1}} (n+1)!. \end{aligned}$$

† Note that the a_n terms represent irrotational flow while the b_n terms yield the vorticity given by (1.4).

With these results, the stream function takes the limiting form

$$\psi = \frac{1-r^2}{2} \left\{ A_0 + \sum_{n=1}^{\infty} A_n r^n e^{in\theta} \right\} \quad \text{for } R \rightarrow 0.$$

This form of the stream function is clearly a biharmonic function. Similarly the vorticity takes the limiting form

$$\omega = 2 \left\{ A_0 + \sum_{n=1}^{\infty} (n+1) A_n r^n e^{in\theta} \right\} \quad \text{for } R \rightarrow 0. \tag{1.9}$$

It is instructive to take a special case for which a solution in closed form may be obtained. Consider a square-wave distribution of velocity along the enclosing streamline

$$u_\theta(1, \theta) = \begin{cases} 1 & \text{for } -\frac{1}{2}\alpha < \theta < \frac{1}{2}\alpha, \\ 0 & \text{for } \frac{1}{2}\alpha < \theta < 2\pi - \frac{1}{2}\alpha. \end{cases} \tag{1.10}$$

The Fourier coefficients for this distribution are

$$A_0 = \alpha/2\pi, \quad A_n = (2/n\pi) \sin \frac{1}{2}n\alpha. \tag{1.11}$$

Then the stream function is given by

$$\psi = \frac{1-r^2}{2} \left\{ \frac{\alpha}{2\pi} + \frac{2}{\pi} \sum_{n=1}^{\infty} \frac{1}{n} r^n \sin \frac{1}{2}n\alpha e^{in\theta} \right\}.$$

Now if the sine is expressed in exponential form, we have ψ expressed as a well-known power series in $r \exp [i(\theta + \frac{1}{2}\alpha)]$ and $r \exp [i(\theta - \frac{1}{2}\alpha)]$. Hence in closed form

$$\psi = \frac{1-r^2}{2\pi} \left[\frac{1}{2}\alpha + \arctan \left\{ \frac{r \sin (\theta + \frac{1}{2}\alpha)}{1-r \cos (\theta + \frac{1}{2}\alpha)} \right\} - \arctan \left\{ \frac{r \sin (\theta - \frac{1}{2}\alpha)}{1-r \cos (\theta - \frac{1}{2}\alpha)} \right\} \right], \tag{1.12}$$

where only the real part of the complex function has been taken.

The velocity components and the vorticity now may be evaluated by differentiating (1.2). However, for Stokes flow, vorticity and pressure are conjugate functions of a complex variable. Hence both real and imaginary parts of (1.9) have physical significance. Proceeding as for the stream function, the vorticity series with the coefficients of (1.11) can be summed. In particular, the vorticity (and hence skin friction) along the enclosing streamline is given by

$$\omega(1, \theta) = \frac{1}{\pi} [\text{ctn } \frac{1}{4}(2\theta + \alpha) - \text{ctn } \frac{1}{4}(2\theta - \alpha)], \tag{1.13}$$

and for the pressure

$$RC_p(1, \theta) = \frac{2}{\pi} \log \left[\frac{1 - \cos (\theta + \frac{1}{2}\alpha)}{1 - \cos (\theta - \frac{1}{2}\alpha)} \right], \tag{1.14}$$

where $C_p = p/\frac{1}{2}\rho\Omega^2a^2$. We note that both skin friction and pressure are singular (the former non-integrably so) at the points of discontinuity in the surface velocity. The solution near these singularities is locally identical to the scraping-corner solution treated by Taylor (1960, 1962), in which an inclined moving wall slides over another fixed wall. Taylor explains this paradoxical situation by arguing that the viscous stress will tend to lift the moving wall, creating a gap and so relieving the corner stresses. However, this explanation does not apply

to the case in which the moving wall recedes from the fluid, since the shear stress reverses its direction in this case. If our circular eddy is regarded as a model for a separated flow, however, the singularity is removed by requiring that the velocity be continuous on the separation streamline. The step-function velocity used here as an example should provide a qualitatively correct model of a separated eddy since the singularities are expected to have only a local effect.

1.3. The Prandtl limit: $R \rightarrow \infty$

For this limit process, the large argument expansion of the Bessel function is appropriate (Whittaker & Watson 1952)

$$I_n(z) = \frac{e^z}{\sqrt{(2\pi z)}} \left\{ 1 + \sum_{r=1}^{\infty} (-1)^r \frac{(4n^2-1)(4n^2-3)\dots[4n^2-(2r-1)^2]}{r!(8z)^r} \right\} + O(e^{-z}/\sqrt{z}).$$

Putting $z = \sqrt{(inR)}$, the coefficient a_n can be written as

$$za_n/A_n = I_n(z)/I_{n+1}(z) = \{(n+1)/z\} + \phi_{n+1}(z), \quad (1.15)$$

where the $\phi_n(z)$ are given by

$$\phi_n(z) \equiv \frac{d}{dz} [\ln I_n(z)] = \sum_{k=0}^{\infty} \frac{C_k(n)}{z^k} + O(e^{-2z}). \quad (1.16)$$

The leading term $C_0(n)$ is dominant in the Prandtl limit, but for later discussion the higher-order terms will be needed. The C_k can be determined directly from the expansion for $I_n(z)$. However, an easier approach may be followed. The function $\phi(z)$ defined above satisfies a differential equation of the generalized Ricatti type

$$\frac{d\phi_n}{dz} + \phi_n^2 + \frac{\phi_n}{z} = 1 + \frac{n^2}{z^2}.$$

Substituting the series expansion (1.16) we find

$$C_0(n) = 1, \quad C_1(n) = -\frac{1}{2}, \quad C_2(n) = (n^2 - \frac{1}{4})/z, \quad (1.17a)$$

while the higher-order coefficients satisfy the recurrence relation

$$2C_k = (k-2)C_{k-1} - \sum_{m=1}^{k-1} C_m C_{k-m}. \quad (1.17b)$$

The dominant term in the expansion is $\phi(z) \sim 1$; consequently

$$a_n \sim A_n/\sqrt{(inR)}.$$

The higher-order terms will be useful in later discussion.

Now consider the b_n -terms; from (1.8)

$$\frac{zb_n I_n(rz)}{A_n} = -\frac{I_n(rz)}{I_n(z)} \frac{I_n(z)}{I_{n+1}(z)} = -\frac{I_n(rz)}{I_n(z)} \left[\frac{n+1}{z} + \phi_{n+1}(z) \right].$$

From the asymptotic expansion for $I_n(z)$, we find

$$\frac{I_n(rz)}{I_n(z)} = \frac{1}{\sqrt{r}} e^{-(1-r)z} F(z) + O(e^{-z}/\sqrt{z}),$$

where $F(z)$ may be expressed as a series of powers in $1/z$, with the leading term unity. Thus the dominant term of the expansion for b_n is given as

$$b_n I_n\{r \sqrt{(inR)}\} \sim -\{A_n/\sqrt{(inRr)}\} e^{-\sqrt{(inR)(1-r)}}.$$

For $r < 1$, the b_n -terms are exponentially small compared with the a_n -terms. This fact has an interesting interpretation: the vorticity perturbation of the flow outside the boundary layer does not appear in an expansion in powers of Reynolds number, but is postponed to the exponentially small terms of the expansion.

Using these limiting expressions, † the dominant terms of a composite expansion for the stream function ($R \rightarrow \infty$) are

$$\psi/r \sim \frac{1}{2}A_0(1-r^2) + \frac{1}{\sqrt{R}} \sum_{n=1}^{\infty} \frac{1}{\sqrt{n}} A_n \left[r^n - \frac{1}{\sqrt{r}} e^{-\sqrt{(inR)(1-r)}} \right] e^{i(n\theta - \frac{1}{4}\pi)}. \quad (1.18)$$

Correspondingly, from (1.4) the vorticity becomes

$$\omega \sim 2A_0 + \sqrt{R} \sum_{n=1}^{\infty} \sqrt{n} A_n \frac{1}{\sqrt{r}} e^{-\sqrt{(inR)(1-r)}} e^{i(n\theta + \frac{1}{4}\pi)} \quad \text{for } R \rightarrow \infty. \quad (1.19)$$

Note that this asymptotic form of the solution is not uniformly valid, holding outside a vanishingly small neighbourhood of $r = 0$. Obviously this limit leads to a boundary-layer type of solution, for which the vorticity diffuses exponentially away from the surface $r = 1$.

The flow is of the type envisaged by Batchelor and others, having a constant vorticity core enclosed by the thin shear layer. The value of the vorticity in the core is proportional to the mean velocity on the boundary streamline. This result is just the linearized version of the exact root-mean-square value derived by Batchelor and was obtained previously by Squire (1956) by consideration of the linearized boundary-layer equations. Note also, that in the limit $R \rightarrow \infty$ the streamlines are concentric circles, in contrast to those of Stokes flow which do not possess this polar symmetry.

On the boundary streamline $r = 1$, (1.19) reduces to

$$\omega(1, \theta) = 2A_0 + \sqrt{R} \sum_{n=1}^{\infty} \sqrt{n} A_n e^{i(n\theta + \frac{1}{4}\pi)} \quad \text{for } R \rightarrow \infty. \quad (1.20)$$

For the A_n given by (1.11) corresponding to the square-wave distribution of velocity $u_\theta(1, \theta)$, the series in (1.20) can be recognized as a combination of generalized Riemann zeta functions as given by Hurwitz's formula (Whittaker & Watson 1952). The result is ‡

$$\omega(1, \theta) = \frac{\alpha}{\pi} + \frac{1}{\pi} \sqrt{(\frac{1}{2}R)} \left[Z\left(\frac{1}{2}, \frac{2\theta + \alpha}{4\pi}\right) - Z\left(\frac{1}{2}, \frac{2\theta - \alpha}{4\pi}\right) \right], \quad (1.21)$$

† These limit processes are not necessarily valid when all terms of the series are present, depending on the rate of convergence of the A_n .

‡ The Hurwitz formula as derived by Whittaker & Watson appears to be limited to Fourier coefficients of order $n^{-(1-s)}$ for $s < 0$. However, if the zeta function used here is regarded as a generalized periodic function in the sense of Lighthill (1962), the Hurwitz formula is applicable for all values of s .

where the periodic function $Z(s, x)$ agrees with the generalized Riemann zeta function in its fundamental period $0 < x < 1$. Equation (1.21) can be written in an alternate form which lends itself to an interesting physical interpretation. Using the conventional series definition of the generalized Riemann zeta function, the difference of two such functions can be expressed as

$$\zeta(s, \xi_1) - \zeta(s, \xi_2) = \sum_0^\infty \left[\frac{1}{(\xi_1 + n)^s} - \frac{1}{(\xi_2 + n)^s} \right].$$

Extending this definition to include $s = \frac{1}{2}$, an individual term of the series is recognized as the effect of one cycle of fluid rotation, the sum taken over all previous cycles in the history of the flow. This cyclic history of the flow causes a

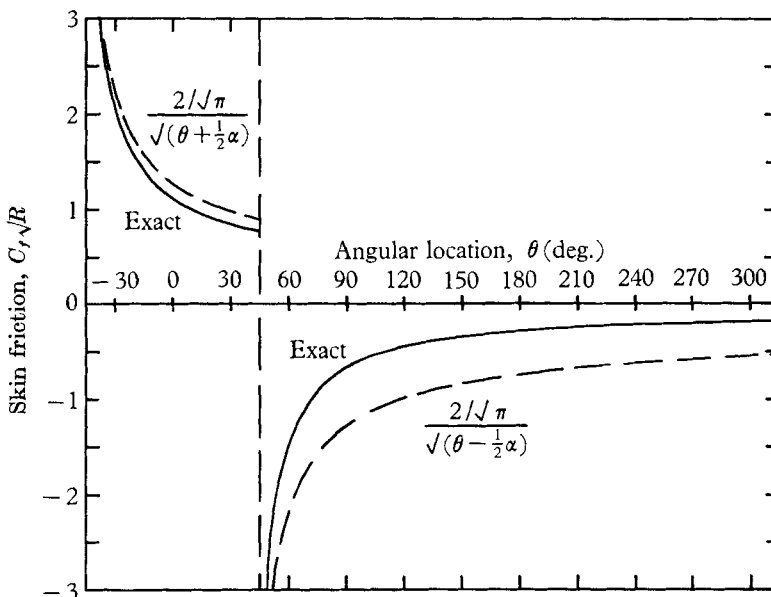


FIGURE 2. Skin-friction distribution in boundary-layer limit for square-wave boundary velocity with $\alpha = \frac{1}{2}\pi$.

thicker viscous layer than for ‘single-pass’ boundary layers. In common with other boundary-layer problems, the skin friction has square-root singularities at the discontinuities of surface velocity ($\theta = \pm \frac{1}{2}\alpha$). The distribution of skin friction for the special case $\alpha = \frac{1}{2}\pi$ is shown in figure 2; the broken curve is the leading term of the above expansion, representing the contribution of the last velocity jump encountered.

The displacement thickness of the boundary layer is also of interest. Introducing the boundary-layer co-ordinate $\eta = \sqrt{R}(1 - r)$, the asymptotic form of the stream function is obtained from (1.18) as

$$\lim_{\substack{R \rightarrow \infty \\ \eta \text{ finite}}} \sqrt{R}\psi = A_0\eta + \sum_1^\infty \frac{1}{\sqrt{n}} A_n [1 - e^{-\sqrt{(in)\eta}}] e^{i(n\theta - \frac{1}{2}\pi)}.$$

The leading term represents a uniform flow outside the boundary layer, the vorticity of the inviscid core being negligible compared with that in the viscous

layer. The series is the excess of volume flux in the boundary layer over that of the uniform flow. Hence, defining a displacement thickness in the usual manner, we have

$$\delta^* = -\frac{1}{\sqrt{R}} \sum_1^{\infty} \frac{1}{\sqrt{n}} \left(\frac{A_n}{A_0} \right) e^{i(n\theta - \frac{1}{4}\pi)}. \quad (1.22)$$

A positive value of δ^* denotes a deficit of volume flux, and hence an effective displacement of the boundary inward toward the centre of the circle. The centre of the inviscid vortex core is shifted accordingly. Let $x = -r \sin \theta$, $y = r \cos \theta$. Then the co-ordinates of the centroid of the shifted inviscid-flow area are (to lowest order in $1/R$)

$$\bar{x} = \frac{1}{\pi} \int_0^{2\pi} \delta^* \sin \theta \, d\theta; \quad \bar{y} = -\frac{1}{\pi} \int_0^{2\pi} \delta^* \cos \theta \, d\theta.$$

Substituting the series form of δ^* , we find that all terms vanish except for $n = 1$; thus

$$\bar{x} = -\frac{1}{\sqrt{R}} \frac{A_1}{A_0} e^{\frac{1}{2}i\pi}; \quad \bar{y} = \frac{1}{\sqrt{R}} \frac{A_1}{A_0} e^{-\frac{1}{2}i\pi}. \quad (1.23)$$

Note that for a symmetric boundary velocity distribution (the A_n all real), the vortex centre is shifted out along a 45° radius, independent of the shape of the distribution. This result holds only for the circular eddy, of course.

For the cosine distribution $A_1 = A_0$, and

$$\delta^* = -(1/\sqrt{R}) \cos(\theta - \frac{1}{4}\pi).$$

Here the inviscid core remains circular as it is shifted off-axis. For other velocity distributions, however, the streamlines of the inviscid core become distorted as a result of the displacement.

1.4. Discussion of results

At this point it is instructive to evaluate the solution for a special case. Although the square-wave distribution of surface velocity permits simple formulae in terms of tabulated functions at the limits of both large and small Reynolds number, the full series is needed for finite values of R . To simplify the calculations, it is desirable to select a single term of the Fourier series for the perturbation velocity; that is, we shall consider a cosine distribution of surface velocity. It will be seen that this distribution is sufficiently general to bring out the salient features of the flow.

Perhaps the most interesting feature of the solution is the change of flow pattern with Reynolds number. This change is characterized by the shift of the vortex centre discussed above. Figure 3 shows the results of calculations† for the cosine distribution $A_0 = A_1 = \frac{1}{2}$. For $R = 0$, the vortex is centred on the line of symmetry $\theta = 0$, consistent with the symmetry of the biharmonic equation and the boundary conditions. The centre is displaced along the line of symmetry toward the point of maximum velocity on the boundary. This condition is a

† For computational purposes, the modified Bessel function $i^n I_n(x\sqrt{i})$ is expressed in terms of its real and imaginary parts $ber_n(x)$, $bei_n(x)$. A short table of these functions is given by Dwight (1961).

result of continuity: the stream tubes must be narrower in the higher-velocity region at the top of the circle ($\theta = 0$). As the inertia of the fluid becomes important, the flow is no longer symmetrical with respect to the boundary conditions. The vortex centre for low Reynolds number is shifted in the direction of the moving boundary. At higher Reynolds numbers, the inertial effects become dominant and the vortex centre becomes aligned with the centre of the circle in the limit $R \rightarrow \infty$.

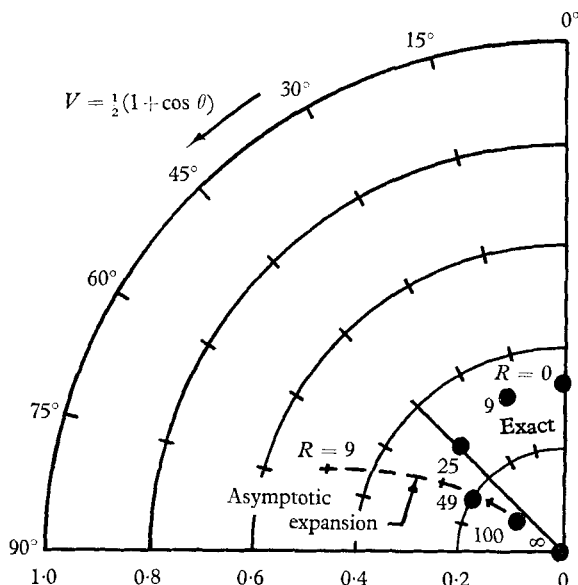


FIGURE 3. Effect of Reynolds number on location of vortex centre for cosine boundary velocity ($A_0 = A_1 = \frac{1}{2}$).

The curve labelled 'asymptotic expansion' in figure 3 corresponds to an expansion for the vortex-core location in powers of $1/R$. Recalling from § 1.3 that the b_n -terms of the stream function are exponentially small for $r < 1$, we have

$$\psi \sim \frac{1}{2}A_0(1 - r^2) + \sum a_n r^n e^{in\theta} \quad \text{for } r < 1,$$

where the real part of ψ is understood. The term in A_0 is the original solid-body rotation, while the series gives the perturbation of the core flow caused by the boundary layer on the wall; the leading term corresponds to a uniform flow, the second term a stagnation flow, and the higher-order terms yield successively more complicated flows necessary to represent the boundary-layer growth and decay. The asymptotic expansion of the a_n was obtained in § 1.3; we have

$$a_n \sim \frac{A_n}{\sqrt{(inR)}} \left\{ 1 + \frac{2n+1}{2\sqrt{(inR)}} + \sum_{k=2}^{\infty} \frac{C_k}{(inR)^{\frac{1}{2}k}} \right\},$$

where the $C_k(n)$ are given by (1.17). For the present case only the a_1 -term appears. The vortex centre then has the co-ordinates r^* , θ^* given by

$$r^* \sim |a_1/A_0|, \quad \tan \theta^* \sim -\text{Im } a_1/\text{Re } a_1.$$

Although this type of expansion is formally correct for sufficiently large R , it is evident from the figure 3 that at moderate R even the qualitative trend is not correct. This result is of significance with regard to practical application of the method of inner and outer expansions (Van Dyke 1964) to separated flows.

The velocity distribution across the circular eddy is shown in figure 4 for several values of Reynolds number. The development of the flow is clearly indicated, from the rounded profile of the fully viscous type ($R = 0$) to the flat

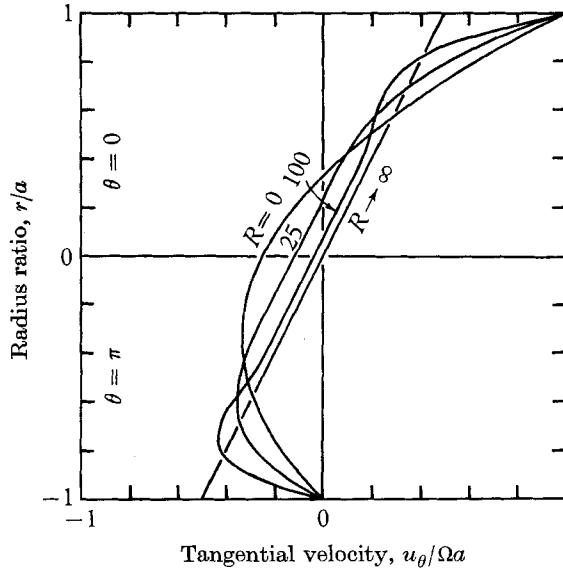


FIGURE 4. Tangential velocity profile on line of symmetry ($\theta = 0$) for cosine boundary velocity ($A_0 = A_1 = \frac{1}{2}$).

profile of inviscid type ($R \rightarrow \infty$). In the inviscid region (the flat part of the profile) the slope appears to be independent of Reynolds number, though the extent of this region varies markedly. This result is consistent with the boundary-layer displacement-thickness model discussed previously. A significant feature of these profiles is the hump which appears near the wall for large R . This persists even in the limit, $R \rightarrow \infty$, in a manner reminiscent of Gibbs' phenomenon for Fourier series. Physically this velocity over-shoot may be explained as the propagation of waves of vorticity from the surface inward through the boundary layer, and may be regarded as the origin of the residual vorticity in the inviscid core. This point illustrates the fundamental difference between recirculating flows and single pass flows. In the former, a fluid particle in the boundary layer on one side of the eddy is accelerated by viscous shear. This added momentum is diffused away from the surface as the flow proceeds around the eddy. On the opposite side of the eddy, the shear retards the flow, setting up a diffusive wave of opposite sign. Hence, the humps in the velocity profile are just the residual effects of the periodic past history of the boundary layer. (The exact analogy of this linearized boundary-layer problem exists for one-dimensional unsteady heat conduction in an infinite slab with periodic surface conditions, and is

discussed in most books on heat-conduction theory; see, for example, Carslaw & Jaeger 1959.)

The power dissipated by the flow may be determined readily. The shear stress on the moving wall is given by

$$\tau_\omega = \mu\Omega\{\omega(1, \theta) - 2V(\theta)\}.$$

The energy dissipated must equal the mechanical work performed by the moving boundary. Hence the power dissipated becomes

$$P = \mu\Omega^2 a^2 \int_0^{2\pi} V(\theta) [\omega(1, \theta) - 2V(\theta)] d\theta.$$

Again restricting ourselves to the pure cosine velocity distribution, substitute the vorticity from (1.4). Carrying out the integration results in

$$P = \frac{1}{2}\pi\mu\Omega^2 a^2 \left\{ \frac{1}{2}\sqrt{iR} \frac{I_1\{\sqrt{iR}\}}{I_2\{\sqrt{iR}\}} - 1 \right\}, \quad (1.24)$$

where the real part is understood. This result holds for any R ; it is of interest to compare this with an expansion in powers of $1/R$. As in (1.15) the quotient of Bessel functions can be expressed as

$$zI_1(z)/I_2(z) = 2 + z\phi_2(z),$$

where $\phi_2(z)$ is given by (1.16) with coefficients from (1.17). Extracting the real part of $\phi\{\sqrt{iR}\}$, the expansion for the power dissipation is

$$(P/\frac{1}{2}\rho\Omega^3 a^4) = \frac{\pi}{2\sqrt{R}} \sum_{n=0}^{\infty} \frac{C_n \cos(n-1)\pi/4}{R^{\frac{1}{2}n}}, \quad (1.25)$$

where the first few C_n are

$$C_0 = 1, \quad C_1 = -\frac{1}{2}, \quad C_2 = \frac{1}{8}, \quad C_3 = \frac{1}{8}, \quad C_4 = \frac{1}{128}, \quad C_5 = -\frac{45}{32}, \dots$$

This is the result which should be obtained by higher-order boundary-layer theory, as in the method of inner and outer expansions. Note that the terms R^{-2} , R^{-4} , R^{-6} , ..., do not appear in the series.

Figure 5 shows the effect of Reynolds number on the power dissipated by the flow, as given by the complete solution (1.24) and by the leading three terms of the expansion in (1.25), labelled first-order, second-order, and third-order boundary-layer theory. We see that the third-order theory is quite good down to a Reynolds number of about 15. Since the next term of the expansion reduces the power dissipation, $R \approx 15$ appears to be the limit of validity of higher-order boundary-layer theory (at least for this problem). By comparing with the results of the vortex-core calculation, it appears that the boundary-layer theory may be extended to lower Reynolds number for integrated quantities, such as average power, than for details of the flow field. The asymptotic variation exhibits the $1/R$ and $1/\sqrt{R}$ behaviour typical of creeping flows and boundary layers, respectively. It is interesting that the power dissipation is given within 10% over the entire range of Reynolds number by the asymptotes, crossing over from the Stokes limit to the Prandtl limit at $R = 8$. This remarkable result is made possible by the undershoot below the boundary-layer limit exhibited in the

figure. A similar result was obtained by the author (unpublished work) for Jeffery–Hamel wedge flow, the cross-over Reynolds number depending on the wedge angle for that case.

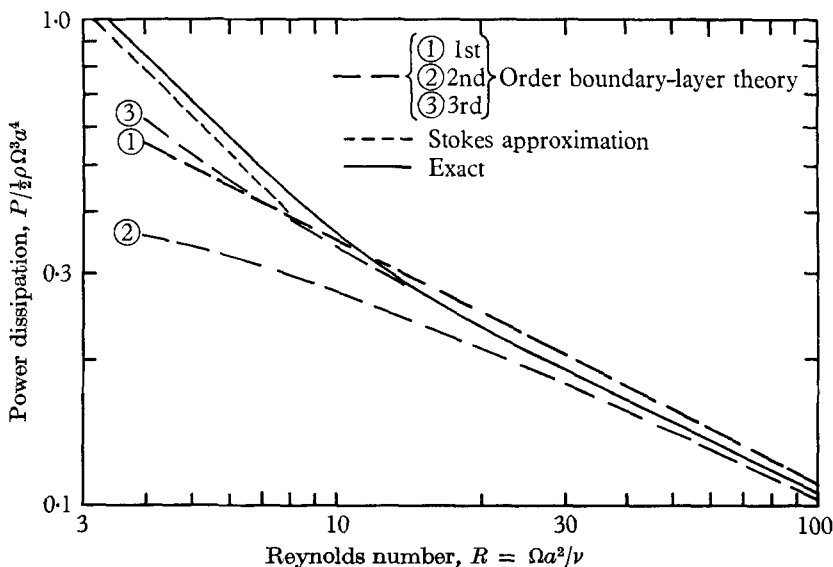


FIGURE 5. Effect of Reynolds number on power dissipation in circular eddy for cosine boundary velocity ($A_0 = A_1 = \frac{1}{2}$).

1.5. Limitations of the analysis

Although the present analysis reveals the development of a separated eddy with arbitrary distribution of velocity on the separation streamline, two major questions arise concerning the validity of the analysis: (1) the circular shape of the eddy permits a constant pressure flow at large Reynolds number and hence may not adequately simulate an eddy of more complicated shape, and (2) unknown non-linear effects may be lost by linearization of the equations of motion. Both of these questions are treated in §2, in which numerical solutions of the full Navier–Stokes equations are obtained for a square cavity. As will be seen, the numerical solutions confirm the linear analysis to a surprising degree; however, certain minor features of the flow are revealed which do not occur in the linear theory for the circle.

An estimate of the effect of the non-linearities can be made rather easily. In the high-Reynolds-number limit, our linearized problem for the circle reduces to the Oseen approximation for a boundary layer on an infinite flat plate with periodic boundary conditions. Now for the boundary layer on a semi-infinite flat plate, it is well known that the Oseen approximation predicts skin-friction values that are 70% too high. However, if the equations are linearized with respect to the mean velocity in the boundary layer, in the manner of Lewis & Carrier (1949), the skin friction is given very accurately. Hence, the effective Reynolds number used in the linear theory should be based on an average velocity rather than on the maximum. Thus when the Reynolds number is based

on the maximum velocity and on the total depth of the cavity rather than the radius, a factor of about 4 should be applied to the values of R appearing in the linear results. It is appropriate here to recall that, according to the linear theory, the inviscid core rotates with the mean velocity of the bounding streamline compared with the root-mean-square value from Batchelor's limit process.

2. Numerical solution of exact equations of motion

2.1. Preliminaries

The analysis presented in § 1 of this study reveals the development of the viscous structure of a recirculating eddy as a function of Reynolds number. However, the analysis was based on a linearized theory, and furthermore restricted to an eddy having a circular boundary. Consequently, certain features of the flow are not expected to be represented properly. The effects of the non-linearity and of non-circular boundaries are assessed now by considering numerical solutions of the full Navier–Stokes equations for a square cavity.

The specific problem considered here is the steady plane flow of an incompressible Newtonian fluid in a square cavity bounded by three motionless walls and by a fourth wall moving in its own plane (see figure 6). Kawaguti (1961) has obtained numerical solutions of this problem for the range of Reynolds number $R = 0$ to $R = 64$ by use of a small digital computer. For a larger Reynolds number ($R = 128$) he was unable to obtain a convergent solution by his iterative procedure. Part 1 of the present work indicates that viscous effects would permeate the entire recirculating flow in this range of Reynolds number. Consequently to confirm or confute the linear theory, calculations at higher Reynolds number are needed. Fortunately, convergent solutions are possible for any Reynolds number by making a minor change in Kawaguti's iteration procedure.

2.2. The difference equations

As indicated in figure 6, we introduce rectangular co-ordinates in the square cavity with origin at the lower left corner. The moving wall of length L is taken at the top, with motion from right to left with velocity V . (This choice is convenient since it results in positive values of the stream function.) Let X and Y be the co-ordinates normalized with respect to L , ($X = x/L$, $Y = y/L$) and Ψ and Ω be the non-dimensional stream function and vorticity, respectively ($\Psi = \psi/LV$, $\Omega = \omega L/V$). Then the vorticity and stream function are related by

$$\nabla^2 \Psi = -\Omega, \quad (2.1a)$$

where $\nabla^2 = \partial^2/\partial X^2 + \partial^2/\partial Y^2$. We now let P be a non-dimensional total pressure ($P = (p_T - p_B)L/\mu V = \frac{1}{2}RC_{p_T}$) with reference to the pressure p_B at the centre of the bottom wall of the cavity. Then the Navier–Stokes equations can be expressed in the form (Lamb 1932)

$$\frac{\partial P}{\partial X} = -R\Omega \frac{\partial \Psi}{\partial X} - \frac{\partial \Omega}{\partial Y}, \quad (2.1b)$$

$$\frac{\partial P}{\partial Y} = -R\Omega \frac{\partial \Psi}{\partial Y} + \frac{\partial \Omega}{\partial X}, \quad (2.1c)$$

where $R = VL/\nu$ is the Reynolds number of the problem.† Note that as $R \rightarrow 0$, equations (2.1*b*) and (2.1*c*) take on the form of the Cauchy–Riemann equations, showing that Ω and P are complex conjugate functions in Stokes flow as discussed in §1. The three equations (2.1) suffice to determine the flow field; however, a simpler set of equations is obtained if the total pressure is eliminated. By cross-differentiating and subtracting (2.1*b*) from (1.2*c*), we obtain the familiar vorticity-diffusion equation

$$\nabla^2 \Omega = R \left[\frac{\partial \Psi}{\partial Y} \frac{\partial \Omega}{\partial X} - \frac{\partial \Psi}{\partial X} \frac{\partial \Omega}{\partial Y} \right]. \tag{2.1*d*}$$

Equations (2.2*a*) and (2.2*d*) will be used to define the flow field; the corresponding pressure distribution then follows from (2.2*b*) and (2.2*c*).

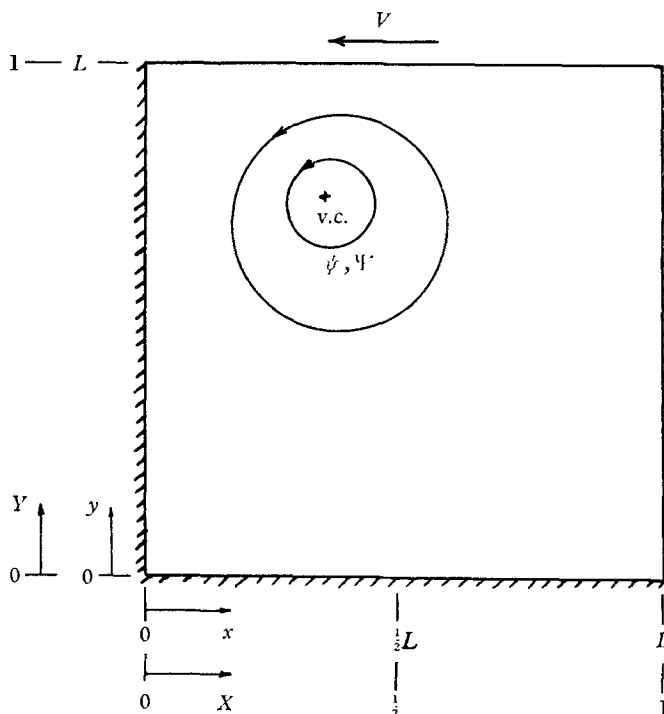


FIGURE 6. Notation for square eddy.

We now propose to replace this set of partial differential equations by a corresponding set of difference equations. Let the square cavity be covered by a lattice having square meshes of dimension h . For an interior point 0 of the lattice, we label the neighbouring points as indicated in figure 7. Then in the usual manner the Laplace operator ∇^2 is replaced by the difference operator H , defined by

$$H\Psi_0 = \Psi_1 + \Psi_2 + \Psi_3 + \Psi_4 - 4\Psi_0.$$

The truncation error associated with this finite-difference operator is of order h^2 ; that is

$$\nabla^2 \Psi - \frac{1}{h^2} H\Psi = O(h^2).$$

† In addition to static and dynamic pressures, the total pressure may include the energy of any scalar potential field.

Other operators having truncation errors of higher order are given by various authors (Collatz 1960); several of these were tried during the course of the study. However, the results using the more complicated operators were not significantly better for the test case at $R = 0$, and for large Reynolds number the computation time was increased. Consequently the formulation given here was used for all the results presented in this paper.

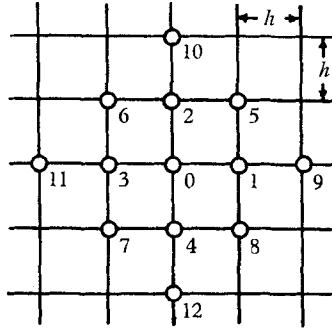


FIGURE 7. Notation for interior lattice points.

Replacing all derivatives in equations (2.1a) and (2.1d) by the difference operator compatible with H , the following set of difference equations is obtained for an arbitrary interior point 0:

$$\Psi_1 + \Psi_2 + \Psi_3 + \Psi_4 - 4\Psi_0 = -h^2\Omega_0, \tag{2.2a}$$

$$\Omega_1 + \Omega_2 + \Omega_3 + \Omega_4 - 4\Omega_0 = \frac{1}{4}R[(\Psi_2 - \Psi_4)(\Omega_1 - \Omega_3) - (\Psi_1 - \Psi_3)(\Omega_2 - \Omega_4)]. \tag{2.2b}$$

In a similar manner, we obtain the difference equations for the total pressure field. Considering the integral of (2.1b) and (1.2c) over a single mesh width, we have

$$P_0 = P_3 - \frac{1}{4}R[\Omega_0(\Psi_1 - \Psi_3) + \Omega_3(\Psi_0 - \Psi_{11})] - \frac{1}{4}[\Omega_2 - \Omega_4 + \Omega_6 - \Omega_7], \tag{2.2c}$$

$$P_0 = P_4 - \frac{1}{4}R[\Omega_0(\Psi_2 - \Psi_4) + \Omega_4(\Psi_0 - \Psi_{12})] - \frac{1}{4}[\Omega_1 - \Omega_3 + \Omega_8 - \Omega_7]. \tag{2.2d}$$

With these equations, knowledge of the flow field permits a point-to-point calculation of the total-pressure distribution within the cavity.

2.3. Boundary conditions

The boundary conditions for the problem stated above are

$$\Psi = \partial\Psi/\partial X = 0 \quad \text{on} \quad X = 0, \quad 0 \leq Y < 1,$$

$$\Psi = \partial\Psi/\partial Y = 0 \quad \text{on} \quad Y = 0, \quad 0 \leq X \leq 1,$$

$$\Psi = \partial\Psi/\partial X = 0 \quad \text{on} \quad X = 1, \quad 0 \leq Y < 1,$$

$$\Psi = 0, \quad \partial\Psi/\partial Y = -1 \quad \text{on} \quad Y = 1, \quad 0 < X < 1.$$

These boundary conditions are treated by introducing a row of image points at a distance h outside the boundary. The values of Ψ are given ($= 0$) at each boundary point, and the values $\tilde{\Psi}$ at the image points are related to those at the interior points by the value of the derivative at the boundary. Thus if the point 0 is taken

as a boundary point on each of the fixed walls, respectively, the values at the image points are

$$\tilde{\Psi}_3 = \Psi_1, \quad \tilde{\Psi}_4 = \Psi_2, \quad \tilde{\Psi}_1 = \Psi_3,$$

respectively. Similarly if Ψ_0 is taken on the moving wall, the image point has the value

$$\tilde{\Psi}_2 = \Psi_4 - 2h.$$

In this way the vorticity on the boundary can be computed from (2.2a); thus for the fixed walls

$$\Omega_0 = \begin{cases} -(2/h^2) \Psi_1 & \text{on } X = 0, \\ -(2/h^2) \Psi_2 & \text{on } Y = 0, \\ -(2/h^2) \Psi_3 & \text{on } X = 1, \end{cases} \quad (2.3a-c)$$

and for the moving wall

$$\Omega_0 = -(2/h^2) (\Psi_4 - h) \quad \text{on } Y = 1. \quad (2.3d)$$

2.4. The relaxation procedure

The difference equations (2.2a), (2.2b) have been solved by a modified relaxation procedure. Defining the residuals $\mathcal{R}(\Psi_0)$, $\mathcal{S}(\Omega_0)$ at the point 0 as the error in the difference equations at a given stage of the approximation, we have

$$\mathcal{R}(\Psi_0) = \frac{1}{4}[\Psi_1 + \Psi_2 + \Psi_3 + \Psi_4 + h^2\Omega_0] - \Psi_0, \quad (2.4a)$$

$$\mathcal{S}(\Omega_0) = \frac{1}{4}[\Omega_1 + \Omega_2 + \Omega_3 + \Omega_4 - \frac{1}{4}R\{(\Psi_2 - \Psi_4)(\Omega_1 - \Omega_3) - (\Psi_1 - \Psi_3)(\Omega_2 - \Omega_4)\}] - \Omega_0. \quad (2.4b)$$

Starting with both Ψ and Ω zero throughout the cavity, the corrected values are then computed from

$$\Psi'_0 = \Psi_0 + K\mathcal{R}(\Psi_0), \quad (2.5a)$$

$$\Omega'_0 = \Omega_0 + K\mathcal{S}(\Omega_0), \quad (2.5b)$$

where the relaxation parameter K has been introduced to afford some control on the iteration procedure. For a well-behaved system, one may choose $K > 1$ to accelerate the convergence of the process. However, Kawaguti's work shows that the iteration procedure for our difference form of the Navier-Stokes equations is not stable at large Reynolds number for $K = 1$. Hence for large R we expect that $K < K^*$, $K^* < 1$, is required for stability; this expectation was confirmed by the computations, with upper and lower bounds on the critical value K^* determined as a function of Reynolds number by trial and error (see table 2, §2.7) K^* appears to be fairly insensitive to mesh size, but strongly dependent on the precise method of iteration used. In each cycle of these calculations, points were taken in each row progressively from left to right, with the rows taken in order from top (moving wall) to bottom; corrected values of Ψ and Ω were used as soon as available. On the other hand, if the corrected values obtained during a given cycle are not used until the following cycle, the value of K^* will be considerably less than the value given in table 2.

Actually the stability requirement $K < K^*$ may be motivated by analogy to the heat-conduction equation. The sequence of values $\Psi^{(n)}$, $\Omega^{(n)}$ may be regarded as a quasi-time dependent problem. $(\frac{1}{4}Kh^2)$ may then be interpreted as a quasi-

time step. As is well known, for stability of the heat-conduction equation the time step must be chosen smaller than a critical value; thus following Collatz (1960) for the one-dimensional problem

$$\frac{1}{4}K = \alpha\Delta t/h^2 \leq \frac{1}{2},$$

<i>R</i>	<i>h</i>	<i>K</i>	\mathcal{R}_{\max}	<i>J</i>	$\Psi_{vc}\dagger$	$\Omega_{vc}\dagger$	$-C_{vc}\dagger$
0	0.100	1.0	5×10^{-6}	61	0.0981	3.029	0
	0.050		5×10^{-6}	164	0.0992	3.152	0
	0.033		5×10^{-6}	348	0.0997	3.179	0
	0.025		1×10^{-6}	663	0.0998	3.200	0
	0.020		1×10^{-6}	1024	0.0998	3.201	0
10	0.100	1.0	1×10^{-6}	79	0.0978	3.028	0.1162
	0.050		1×10^{-6}	234	0.0994	3.155	0.1378
	0.033		1×10^{-6}	499	0.0999	3.187	0.1465
	0.025		1×10^{-6}	856	0.1000	3.205	0.1493
	0.020		1×10^{-6}	1030	0.0999	3.204	0.1482
100	0.100	0.7	5×10^{-6}	117	0.0784	2.854	0.0850
	0.050		1×10^{-6}	498	0.0955	3.136	0.1561
	0.033		5×10^{-6}	762	0.0999	3.150	0.1745
	0.025		5×10^{-6}	1282	0.1015	3.143	0.1810
	0.020		$3 \times 10^{-6}\ddagger$	2000 \ddagger	0.1022	3.145	0.1841
200	0.100	0.7	5×10^{-6}	106	0.0563	2.486	0.0364
	0.050	0.7	5×10^{-6}	375	0.0868	2.639	0.1398
	0.033	0.5	5×10^{-6}	1302	0.0987	2.605	0.1775
	0.025	0.5	5×10^{-6}	2236	0.1032	2.607	0.1906
400	0.100	0.5	5×10^{-6}	137	Oscillations in solution		
	0.050	0.4	5×10^{-6}	632	0.0675	2.170	0.0932
	0.033	0.4	$9 \times 10^{-6}\ddagger$	1500 \ddagger	0.0923	2.080	0.1531
	0.025	0.5	5×10^{-6}	2407	0.1017	2.142	0.1793
700	0.100	0.1			Divergent		
	0.050	0.3	5×10^{-6}	1378	0.0414	5.410	—
	0.033	0.3	$2.4 \times 10^{-5}\ddagger$	3000 \ddagger	0.0783	1.799	0.1184
1000	0.100	0.2	$1.3 \times 10^{-6}\ddagger$	1000 \ddagger	—	—	—
	0.050	0.3	$2 \times 10^{-5}\ddagger$	800 \ddagger	—	—	—
	0.025	0.2	$6 \times 10^{-4}\ddagger$	500 \ddagger	—	—	—

† See figure 11 for co-ordinates of vortex centre.

‡ These cases were terminated by the pre-selected number of iterations.

TABLE 2. Properties of finite-difference solutions

where α is the thermal diffusivity in the heat-conduction equation. (For the two-dimensional problem, a similar analysis leads to $K \leq 1$.)† This value cannot be applied to the Navier–Stokes equations, of course, since the analogy is far from exact. However, the qualitative behaviour appears correct.

† This result is for the ‘explicit method’, in which the time derivative is represented by the forward difference. It is well known to numerical analysts that the ‘implicit method’ in which the time derivative is represented by a backward difference, is inherently more stable. Hence in our calculations, use of corrected values in the mesh as soon as available corresponds to a mixture of explicit and implicit methods, allowing a larger value of K^* .

2.5. Limiting solutions for a square

Before proceeding with the description of the numerical results, the limiting forms of the solution should be considered. In the Stokes limit ($R \rightarrow 0$) the governing equations (2.1) reduce to the biharmonic equation. For a rectangular boundary, this equation can be solved by elementary methods for certain types of boundary conditions common in the literature of elasticity. For the conditions of the present problem, an analytical solution in closed form is not possible by standard methods. However, the square cavity was treated by following the work of Muskhelishvili (1963), employing conformal mapping procedures. To obtain a solution, the mapping function was approximated by a finite number of terms of its infinite series, providing a polynomial approximation to the solution in the transformed variable. By comparing solutions truncated at different number of terms, it was decided that accuracy obtained by this method is worse than that of finite-difference solutions. Hence the analysis is not presented here.

The high-Reynolds-number limit ($R \rightarrow \infty$) is more important, since it cannot be attained directly by the numerical programme. According to the uniform vorticity model, the stream function must satisfy the following Poisson equation

$$\nabla^2(\Psi/\Omega) = -1. \tag{2.6}$$

The stream function must vanish along the boundary, velocity slip at the wall permitted by the thin boundary layer in the limit $R \rightarrow \infty$. Hence for a square cavity we require

$$\Psi = 0 \quad \text{on} \quad \left\{ \begin{array}{l} X = 0, \quad X = 1 \quad \text{for} \quad 0 < Y < L, \\ Y = 0, \quad Y = 1 \quad \text{for} \quad 0 < X < L. \end{array} \right\}$$

This problem is solved easily by use of the finite Fourier transform, defined as

$$\bar{\Psi} = \int_0^1 \Psi(X, Y) \sin(\rho\pi X) dX. \tag{2.7}$$

The solution then becomes

$$\Psi = 2 \sum_{\rho=1}^{\infty} \bar{\Psi}(Y, \rho) \sin(\rho\pi X). \tag{2.8}$$

By use of (2.7) the differential equation (6.2) is transformed to

$$\frac{d^2 \bar{\Psi}}{dY^2} - (\rho\pi)^2 \bar{\Psi} = -\frac{\omega a}{\rho\pi} [1 - (-1)^\rho]. \tag{2.9}$$

Solving this equation subject to the prescribed boundary conditions, leads to the following form for the stream function

$$\Psi(X, Y) = \frac{4\Omega}{\pi^3} \sum_{\rho=1}^{\infty} \frac{[1 - (-1)^\rho]}{2\rho^3} [\tanh \frac{1}{2}\rho\pi \sinh \rho\pi Y - (\cosh \rho\pi Y - 1)] \sin \rho\pi X. \tag{2.10}$$

By differentiation, the velocity components may be obtained. In particular, the inviscid flow velocity at the surface is

$$\left(\frac{u_0}{\omega L}\right) = \frac{1}{\Omega} \left[\frac{\partial \Psi}{\partial Y}\right]_{Y=0} = \frac{4}{\pi^2} \sum_{\rho=1}^{\infty} \frac{1}{\rho^2} \left[\frac{1 - (-1)^\rho}{2}\right] \tanh \frac{1}{2}\rho\pi \sin \rho\pi X. \tag{2.11}$$

Now by making use of the equality ($0 \leq X \leq 1$),

$$\sum_{n=1}^{\infty} \frac{1}{(2n-1)^2} \sin(2n-1)\pi X = \int_0^{\frac{1}{2}\pi X} \log(\theta \cot \theta) d\theta + \frac{1}{2}\pi X [1 - \log \frac{1}{2}\pi X],$$

the series can be rewritten in a form more convenient for calculations

$$\left(\frac{u_0}{\omega L}\right) = \frac{4}{\pi^2} \left\{ \int_0^{\frac{1}{2}\pi X} \log(\theta \cot \theta) d\theta + \frac{1}{2}\pi X [1 - \log \frac{1}{2}\pi X] - \sum_{\rho=1}^{\infty} \frac{1}{(2\rho-1)^2} [1 - \tanh \frac{1}{2}(2\rho-1)\pi] \sin(2\rho-1)\pi X \right\}. \quad (2.12)$$

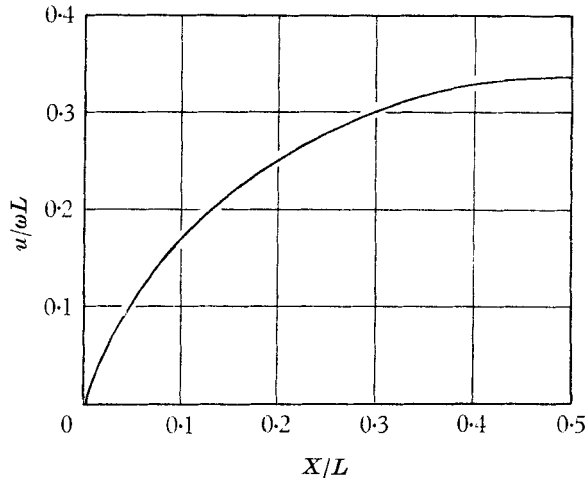


FIGURE 8. Inviscid velocity distribution on boundary of square eddy.

Note that the modified series converges extremely rapidly, only two or three terms giving sufficient accuracy for graphing. The resulting values of inviscid velocity are plotted in figure 8. It is noteworthy that no change of sign occurs; that is, no secondary eddies exist. As will be seen, this result is the most serious failure of the uniform vorticity model. From Batchelor's model (assuming the pressure gradient to have no influence on the mean value, the root-mean-square of the velocity is constant across the viscous layer. At the surface the mean-square value is just $\frac{1}{4}V^2$; hence squaring the series in (2.11) and integrating

$$V^2 = \frac{4}{L} \int_0^1 u^2 dx = \frac{32}{\pi^4} \omega^2 L^2 \sum_{n=1}^{\infty} \frac{1}{(2n-1)^4} \tanh^2 \frac{1}{2}(2n-1)\pi \simeq 0.28116 \omega^2 L^2.$$

Thus in the inviscid limit $\Omega \rightarrow 1.886$.

For later convenience, we also obtain the velocity distribution on the vertical centreline of the square. From (2.10) we find

$$\left(\frac{u_{\frac{1}{2}}}{V}\right) = \left[\frac{\partial \Psi^*}{\partial Y}\right]_{X=\frac{1}{2}} = \frac{4\Omega}{\pi^2} \sum_{\rho=1}^{\infty} \frac{1}{\rho^2} \left[\frac{1 - (-1)^\rho}{2}\right] [1 - \operatorname{sech} \frac{1}{2}\rho\pi] \cos \rho\pi Y.$$

Summing the first term gives

$$\frac{1}{\Omega} \left(\frac{u_{\frac{1}{2}}}{V}\right) = \left(\frac{1}{2} - Y\right) - \frac{4}{\pi^2} \sum_{n=1}^{\infty} \frac{1}{(2n-1)^2} \operatorname{sech} \frac{1}{2}(2n-1)\pi \cos(2n-1)\pi Y. \quad (2.13)$$

The series in (2.13) is rapidly convergent, so that this form is convenient for calculations. Note that the series expresses the deviation from solid-body rotation, caused by the square boundary.

2.6. Numerical results

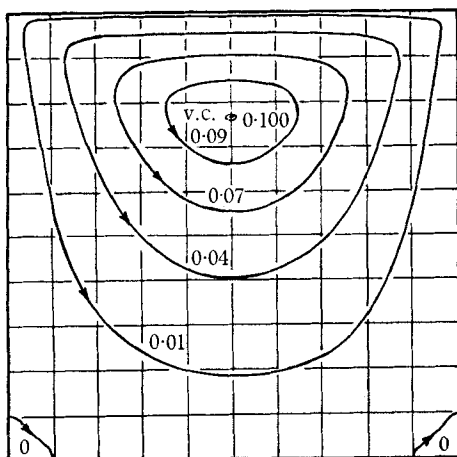
The relaxation calculations were carried out on an IBM 7094 digital computer, using floating-point arithmetic. After an exploratory period during which various finite-difference formulations were used, the procedure outlined previously was settled upon as being a satisfactory method, characterized by simplicity of program logic, speed of calculation, and stability of the iterated computations. The program was then modified to include an integration subroutine to compute the total pressure distribution from equations (2.1), using the final iterated flow field. In addition, interpolation routines were added to determine the vortex centre and to compute automatically the loci of constant values of the stream function, vorticity, total pressure, and later, the temperature. (An automatic plotter became available during the course of the study, but was not used since most of the calculations had been completed.) The relaxation portion of the program was arranged so that computations are terminated when the maximum residual \mathcal{R}_{\max} in the mesh is reduced below a predetermined value, or when the number of iterations J exceeds a predetermined value; $\mathcal{R}_{\max} \leq 5 \times 10^{-6}$ was usually required for convergence. However, the number of iterations required for this degree of convergence increased drastically with Reynolds number. This effect is clear from table 2 (see § 2.4), which summarizes the conditions covered by the calculations.

As indicated by table 2, stable solutions were obtained for Reynolds numbers as high as 1000, the highest value attempted. However, as Reynolds number increases, the convergence parameter K decreases, thus increasing the iterations, and simultaneously the mesh size must be decreased to attain the same degree of accuracy, owing to the diminishing thickness of the viscous layer. Hence the computing time becomes excessive for large R . In this study the maximum machine time allowed for one case was arbitrarily set at about 30 min.; this limitation permitted accurate solutions to be obtained for $R \leq 400$, which is sufficient for our present purposes.†

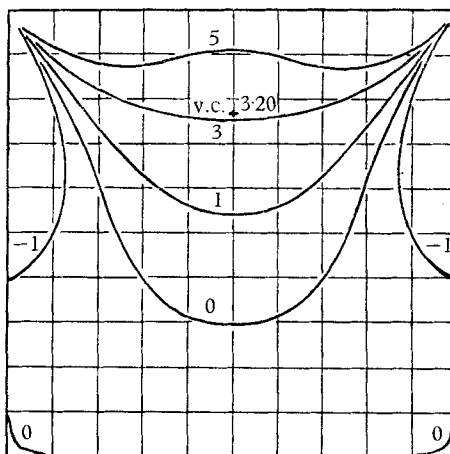
Consider now the properties of the convergent solutions. The solutions discussed here are representative of the most accurate solution obtained for each case; the question of convergence with respect to both iteration and mesh size is deferred to § 2.7.

The development of the flow with Reynolds number is shown in figure 9 at three conditions: $R = 0, 100, 400$. The streamline pattern (figure 9(a)) is only slightly affected by Reynolds number; however, the shift of vortex centre with increasing R is clearly evident, first in the downstream direction (of the moving

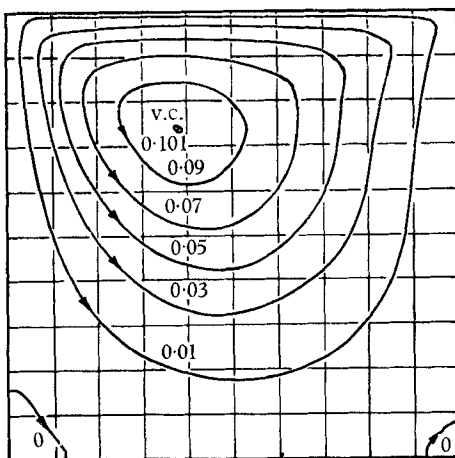
† The running time in minutes of the present FORTRAN program on an IBM 7094 computer can be calculated as $5J/h^2 \times 10^{-6}$. Although this performance could be improved considerably, no such attempt was made since an improvement by at least an order of magnitude would be required to obtain accurate solutions at a significantly higher Reynolds number, say $R = 1000$.



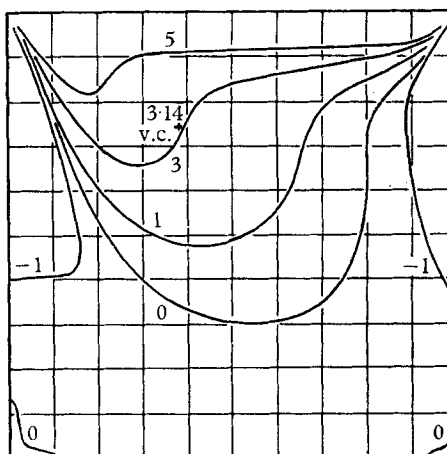
$R = 0$



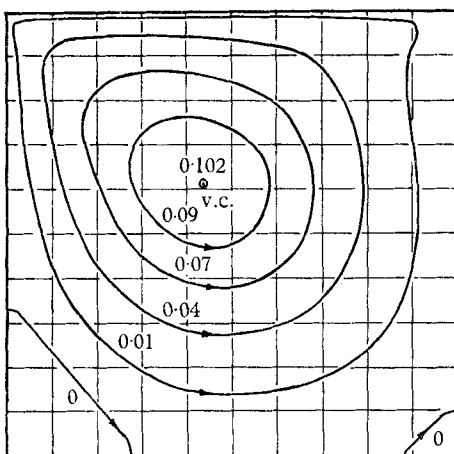
$R = 0$



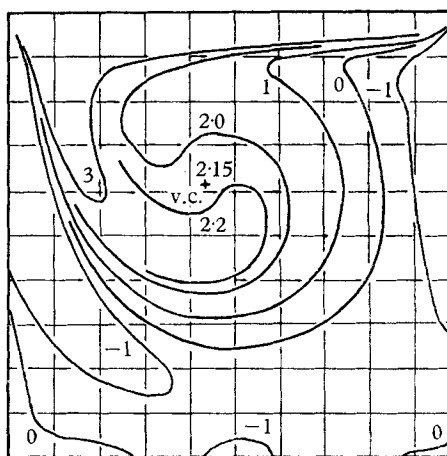
$R = 100$



$R = 100$



$R = 400$

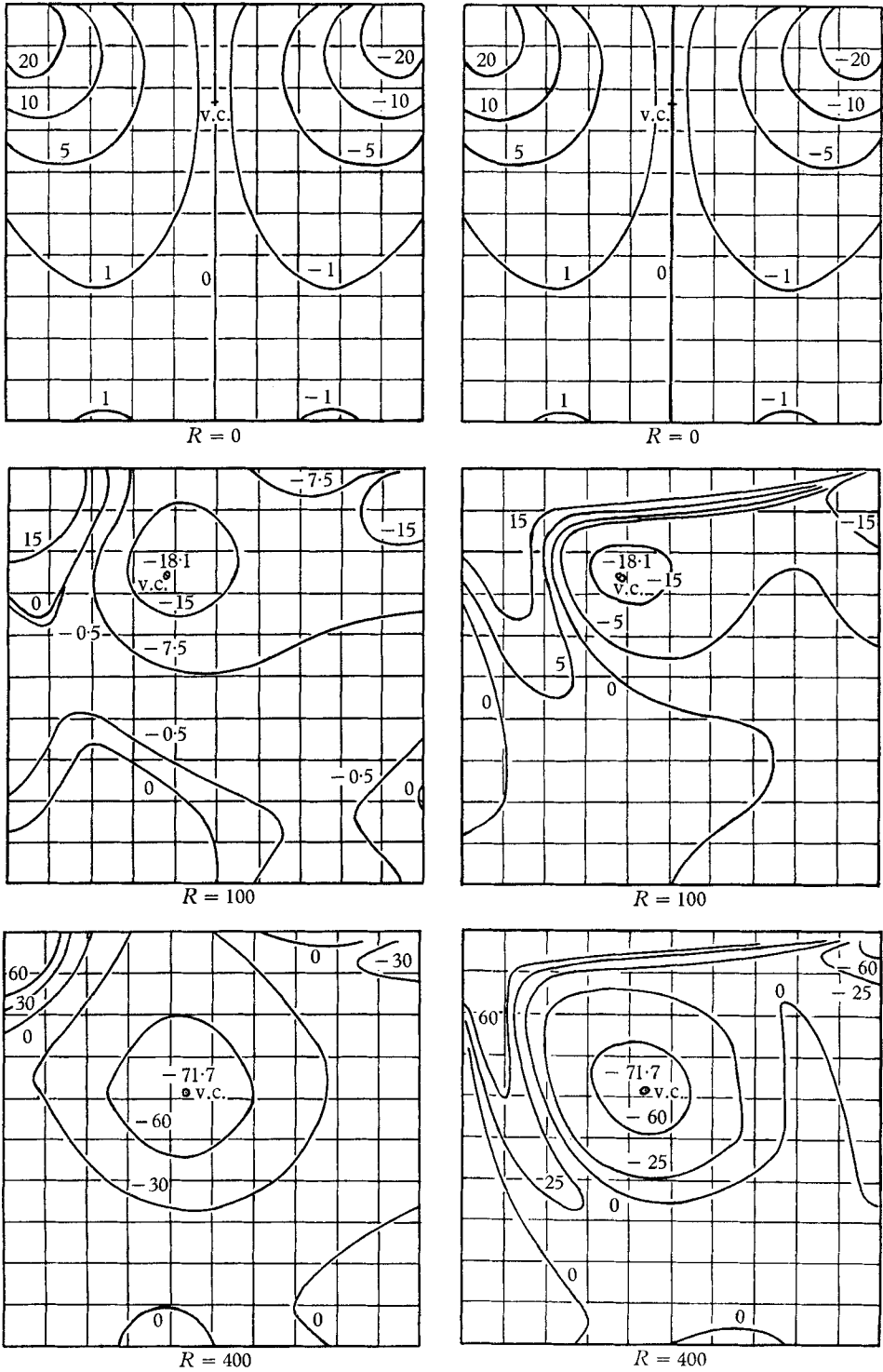


$R = 400$

(a) Streamlines

(b) Vorticity

FIGURE 9. For title see facing page.



(c) Static pressure

(d) Total pressure

FIGURE 9. Properties of viscous eddy in square for $h = 0.025$.

boundary) and then toward the centre of the square. This trend shown by the numerical results for the square is remarkably similar to that of the analytical solution for the circle, as shown in figure 3, especially if the Reynolds number of the linearized analysis is modified by the factor of 4 suggested in § 1.

The vorticity distribution (figure 9(b)) provides a stronger measure of the effect of viscosity. The symmetric pattern at $R = 0$ is due to the vanishing of the convection terms in (2.1d). However at $R = 400$ these terms have begun to dominate the flow, producing a core of nearly uniform vorticity. Note the strong variation of vorticity in the boundary layer, especially evident along the top and left side of the cavity. The interaction of convection and viscous diffusion of vorticity in the viscous annulus is indicated by the 'stretching' of the contours in the direction of flow. Note that the value of vorticity at the vortex centre, indicated by 'v.c.' in figure 9, ranges from $\Omega = 3.20$ at $R = 0$, 3.14 at $R = 100$, to 2.15 at $R = 400$; this sequence compares well with the limiting value $\Omega = 1.89$ obtained by use of Batchelor's model.

The static and total pressure contours are shown in figures 9(c) and 9(d). In the completely viscous limit, the static and total pressure become identical and show no resemblance to the streamlines. Since the pressure is then a harmonic function, the contours cannot be closed but must end on the boundaries. Conversely, for the inviscid limit, total pressure is conserved on streamlines, so that the contours of total pressure should become identical to the streamlines. This development from fully viscous to inviscid flow is indicated clearly by figure 9(d).

At $R = 100$, a very small inviscid core has developed around the vortex centre, while at $R = 400$, the inviscid core has grown to a diameter about $\frac{1}{3}$ that of the cavity.† From these plots, we conclude that the total pressure distribution is the best indicator of the degree of viscous and inviscid flow. The interaction of convection and viscous diffusion of total pressure along the streamlines is indicated just as for vorticity. Actually, in steady flow, the total pressure obeys a diffusion equation with a 'source' term representing a viscous loss proportional to the square of the vorticity,

$$Dp_T/Dt = \nu \nabla^2 p_T - \mu \omega^2.$$

Hence, in regions of highly rotational flow, the total pressure 'streamers' must be shorter than in those of small vorticity. This effect can be seen by comparing figures 9(b) and 9(d). It is also interesting to note that in the upper corners the static pressure retains its asymmetric singularities over the entire range of Reynolds number, even though taking on a symmetric distribution in the main body of the flow.

A striking feature of the flow field is the growth of the secondary eddies appearing in the bottom corners of the cavity (figure 9(a)). These triangular-shaped eddies, present at all Reynolds number, have a diameter of about 10% that of the cavity at $R = 0$. However, at $R = 400$, the upstream eddy has grown to about $\frac{1}{3}$ the diameter of the cavity, although the downstream eddy is relatively

† The thickness of the viscous layer for values of Reynolds number as high as 400 is explained by the infinitely long history of recirculation, as discussed in § 1. It may be noted that the boundary-layer thickness is given quite accurately by the linear theory of § 1.

unaffected by Reynolds number. † Moffatt (1964) has shown that a self-similar solution of Dean & Montagnon (1949) for Stokes flow in a corner exhibits secondary eddies of this type. Assuming a solution of the form

$$\Psi = r^\lambda g(\theta),$$

where r is radius and θ the polar angle measured from the corner, Dean showed that λ is real for the interior angle of the corner α greater than a critical value $\alpha^* \approx 123^\circ$. For more acute angles, λ becomes complex. Moffatt pointed out the physical significance of this result; namely, for $\alpha < \alpha^*$ an infinite sequence of contra-rotating eddies exists in the corner, the size and strength of these eddies vanishing as the corner is approached. For $\alpha > \alpha^*$ the flow does not re-circulate. It is of interest to compare the secondary eddy of the present numerical solution with the self-similar solution of Dean & Montagnon for $R = 0$. Following Moffatt (and correcting an obvious error) the separation streamline between adjacent eddies is given by the equation

$$r = r_0 \exp \left\{ -(1/q) [\phi(\theta) - \frac{1}{2}\pi + n\pi] \right\}$$

$$\phi(\theta) = \arg \{ \cos \lambda \theta \cos (\lambda - 2) \alpha - \cos (\lambda - 2) \theta \cos \lambda \alpha \},$$

where r_0 is an arbitrary scale factor, and $\lambda = (1 + p) + iq$, where $p \simeq 8.60/\pi$ and $q = 3.54/\pi$ for a right-angle corner. We represent the internal structure of the eddy by the contour $\Omega = 0$, which may be expressed by a similar equation

$$r = r_1 \exp \{ (1/q) [\text{arc tan} (\tanh q\theta \tan (p - 1) \theta)] \},$$

where r_1 is the radius of the contour $\Omega = 0$ on the centreline $\theta = 0$ of the corner. Either of the scale factors r_0 and r_1 may be chosen arbitrarily, the other then being fixed by requiring the separation streamline and the zero-vorticity contour to coincide on the walls. For purposes of comparison, the free scale factor is chosen to make the separation streamline coincide on the corner centreline $Y = X$ with that obtained from the relaxation solution. The comparison is shown in figure 10 for the large corner eddy at $R = 400$. The agreement is seen to be very good, indicating that the secondary eddy is completely viscous in nature, even though the primary eddy is predominantly inviscid. This conclusion is borne out by the magnitude of a Reynolds number R_2 characteristic of the secondary eddy, defined for convenience in terms of the circulation around the secondary eddy ($R_2 = \Gamma/\nu$). Integrating the vorticity over the area of the secondary eddy yields $R_2 \approx 1.6$. This side-by-side existence of an eddy accurately described by Stokes flow with a nearly inviscid primary flow is one of the more interesting results of this study. Of course, at sufficiently high Reynolds number, the secondary eddy also would become inviscid in accordance with Batchelor's theorem for recirculating flows, viscous effects contracting further in the hierarchy of corner eddies.

The structure of the flow in the primary eddy is shown most clearly by a graph of the velocity profile across the eddy. In figure 11, velocity profiles are compared

† The terms upstream and downstream here refer to the flow in the primary eddy, not the moving wall.

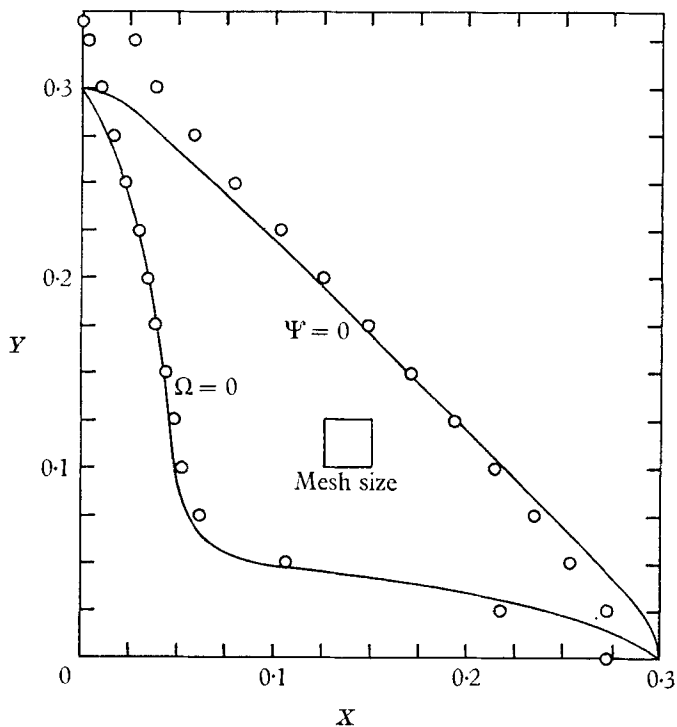


FIGURE 10. Structure of secondary eddy. — Self-similar Stokes flow; \circ , relaxation solution for square ($R = 400$, $h = 0.025$).

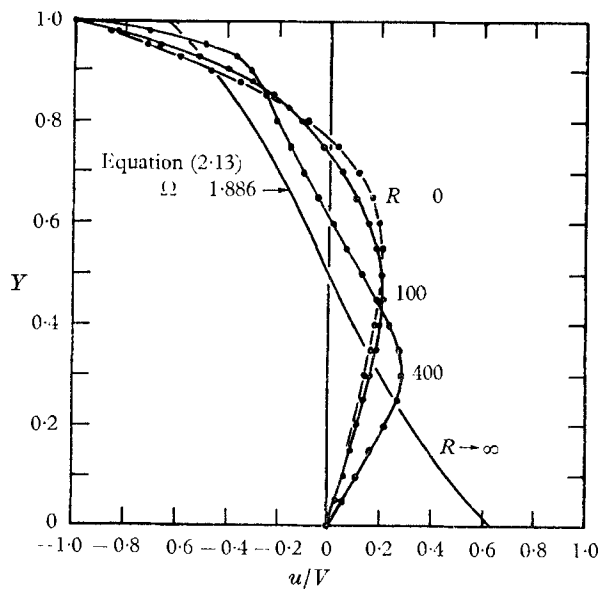


FIGURE 11. Velocity profiles on vertical centreline of square eddy.

for several values of Reynolds number, together with that for the uniform vorticity model, here labelled $R = \infty$. The trend from the rounded profile for $R = 0$ to the flattened profiles at high Reynolds number is clear. By comparing these results with figure 4, it is seen that the dominant features of the flow in the primary eddy are predicted with remarkable fidelity by the linearized analysis (again recall the factor of 4 on Reynolds number owing to the different definition of R and to the use of a mean velocity in the linearization). Note in particular the thinning of the boundary layer with increasing R and the velocity overshoot near the upper wall at $R = 400$. In contrast to the linear theory, however, it seems clear that the

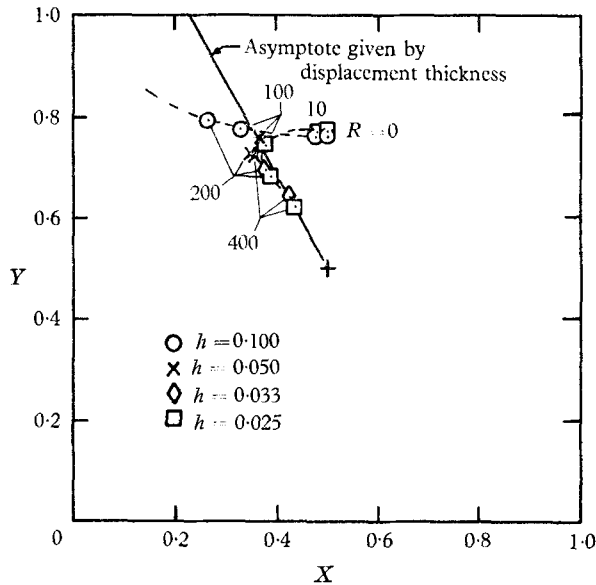


FIGURE 12. Effect of Reynolds number and mesh size on location of vortex centre.

growth of the secondary eddy in the bottom of the square cavity will prevent the vortex centre from approaching the geometric centre of the cavity. It was found that for large R the mesh size has a strong influence on the location of the vortex centre (as well as on the entire flow field) as indicated in figure 12. Since convergence of the finite difference solutions is involved, the discussion of the vortex centre is deferred to the following section.

2.7. Validity of the finite-difference solutions

In obtaining the results presented here, it became apparent that completely misleading results could be obtained unless exceptional care is taken regarding convergence of the numerical solution. This question of convergence has several parts:

- (a) How small a mesh must be chosen to ensure accuracy to the desired number of decimal places.
- (b) For given mesh, to what magnitude must the residuals be reduced.
- (c) When using a fine mesh, how many significant figures must be carried, owing to the small differences of the function relaxed.

Taking these questions in reverse order, eight significant figures were carried in all calculations, in order to obtain a solution accurate to 4 significant figures. By evaluating the differences at typical points of the solutions obtained, it was determined that this degree of precision is sufficient for a mesh of up to about 50×50 points. For a finer mesh the differences become so small that the convergence criterion used ($|\mathcal{R}| < 10^{-6}$, for example) can be satisfied for 'solutions' of less than the desired degree of accuracy.

The choice of residual size for convergence was empirical; by observing the change of solution as the residuals were reduced, it was possible to estimate a satisfactory cut-off value of \mathcal{R} . (It should be mentioned that after the first several iterations, the maximum residuals were reduced very slowly, changing sign periodically, with a period of the order of 200 to 500 iterations, depending on the Reynolds number.) Convergence with mesh size was checked by comparing calculations for various h . Table 2† contains results for several quantities evaluated at the vortex centre. Thus, comparing values of Ψ_{vc} and Ω_{vc} it is evident that convergence to 4 decimal places has been achieved except at the highest Reynolds numbers. At $R = 400$, the accuracy becomes somewhat questionable, although extrapolation of Ψ_{vc} to $h = 0$ indicates a deviation of the order of 10%. It is remarkable that the vorticity is quite insensitive to h for all values of R . Note also the trend toward the theoretical limit $\Omega = 1.886$ as $R \rightarrow \infty$.

In addition to the variation of the level of values, the entire flow field is strongly affected by mesh size for the larger values of R . This effect is illustrated in figure 12, in which the co-ordinates of the vortex centre are plotted as a function of Reynolds number for the various values of h . It is clear from the figure that completely erroneous conclusions can be drawn if the mesh size is too coarse. For example, results for the 10×10 mesh used by Kawaguti indicate that the vortex centre approaches the downstream corner of the moving wall monotonically with increasing R , while from table 2, the values of Ψ_{vc} would indicate a progressively weaker flow recirculation. However, for a finer mesh, the vortex centre instead approaches the centre of the square for large R , just as for the circular eddy of § 1, and the strength of the flow field (Ψ_{vc}) remains practically constant. These results emphasize the importance of a careful evaluation of the convergence of numerical solutions.

The line drawn from the centre of the square in figure 12 is the asymptote of the vortex centre calculated from the linear theory of § 1, by evaluating the displacement thickness of the boundary layer on the boundary of the square. The good agreement with the numerical results for a fine mesh is surprising in view of the large secondary eddy at the bottom of the square cavity.

2.8. *The thermal problem*

The distribution of thermal energy within the recirculating flow is closely analogous to that of vorticity. Owing to the different boundary conditions, the distributions of temperature and vorticity within the boundary layer must differ, but in the limit $R \rightarrow \infty$, both will tend to become uniform as the inviscid core

† See § 2.4.

develops (see below). We now consider the detailed development of the thermal field corresponding to the flow field solutions already discussed.

Following Howarth (1953), the energy equation for a fluid of constant density may be written in the form

$$\rho c_p DT/Dt = \nabla(\kappa \nabla T) + \mu \Phi, \quad (2.14)$$

where c_p is the specific heat at constant pressure, κ the coefficient of thermal conductivity, and Φ the dissipation function. In the Navier–Stokes formulation for plane two-dimensional flow

$$\Phi = 2 \left[\left(\frac{\partial u}{\partial x} \right)^2 + \left(\frac{\partial v}{\partial y} \right)^2 \right] + \left[\frac{\partial v}{\partial x} + \frac{\partial u}{\partial y} \right]^2. \quad (2.15)$$

Consider the integral of (2.14) around the closed streamlines. Putting ξ , η as orthogonal streamline co-ordinates and W as the magnitude of the velocity, the operator D/Dt becomes $(W/h_1)(d/d\xi)$ for steady flow. We shall assume a fluid for which the properties c_p , κ , and μ are constant. Hence we find

$$\oint \{ \nabla^2 T + (\mu/\kappa) \Phi \} \frac{h_1 d\xi}{W} = 0, \quad (2.16)$$

which holds on any closed streamline for any value of Reynolds number. Now in the inviscid limit ($R \rightarrow \infty$ holding Prandtl number fixed), (2.14) implies that the temperature is constant along streamlines; i.e. $T = T(\psi)$. Then noting

$$W = \frac{1}{h_2} \frac{d\psi}{d\eta},$$

and
$$\omega = -\nabla^2 \psi = -\frac{1}{h_1 h_2} \frac{\partial}{\partial \eta} \left(\frac{h_1 d\psi}{h_2 d\eta} \right) = -\frac{1}{h_1 h_2} \frac{\partial}{\partial \eta} (h_1 W),$$

we find
$$\nabla^2 T = W^2 T''(\psi) - \omega T'(\psi). \quad (2.17)$$

The circulation Γ is given by

$$\Gamma(\psi) = \oint h_1 W d\xi,$$

so
$$\Gamma'(\psi) = \oint \frac{\partial}{\partial \psi} (h_1 W) d\xi = -\oint \frac{\omega h_1}{W} d\xi.$$

This result, together with (2.17), allows the integral condition (2.16) to be written in the form

$$\frac{d}{d\psi} [\Gamma(\psi) T'(\psi)] = -\frac{\mu}{k} \oint \frac{h_1 \Phi}{W} d\xi. \quad (2.18)$$

For circular streamlines (solid body rotation), the dissipation function vanishes identically. Hence the integral in (2.18) is zero, and (since $\Gamma = 4\pi\psi$ for that case) we may integrate to obtain

$$T(\psi) = A + B \int \frac{d\psi}{\Gamma(\psi)} = A + \frac{B}{4\pi} \ln \psi.$$

If the vortex centre occurs inside the flow field (singly connected region), $B = 0$ and the temperature of the inviscid core is distributed uniformly. Now consider non-circular streamlines: if we consider the flow to be solid-body rotation plus

a perturbation due to non-circular boundaries, Φ is of second order in that perturbation. Consequently, even for a non-circular eddy, the temperature of the inviscid core will be uniform to first order.†

The thermal structure of the eddy at finite Reynolds number can be studied by a linearized analysis as carried out in § 1 for the flow field, with similar results for the development of the thermal boundary layer. The dissipation function vanishes in such a first-order treatment, so that temperature and vorticity are exact analogues. Since no new results are gained by such an analysis, we turn instead to the 'exact' finite-difference solutions of the energy equation.

Referring to figure 7, we define the residual $\mathcal{J}(T_0)$ as the error at the point 0 of the difference equation corresponding to (2.14)

$$\mathcal{J}(T_0) = \frac{1}{4}[T_1 + T_2 + T_3 + T_4] - T_0 - \frac{1}{16}\sigma R[(\Psi_2 - \Psi_4)(T_1 - T_3) - (\Psi_1 - \Psi_3)(T_2 - T_4)] \\ + (\sigma V^2/4h^2c_p) [\frac{1}{4}(\Psi_5 + \Psi_7 - \Psi_6 - \Psi_8)^2 + (\Psi_1 + \Psi_3 - \Psi_2 - \Psi_4)^2]. \quad (2.19)$$

Then at each stage of the iterative calculation, corrected values are computed from

$$T'_0 = T_0 + K\mathcal{J}(T_0).$$

For convenience the relaxation parameter was taken to be that for the flow field calculations, and the relaxation process for T was carried out simultaneously with that for the flow field.

Calculations were carried out for two cases, depending on the heat transfer at the fixed walls. Case A is characterized by a large temperature difference between fixed and moving walls, so that the dissipation term is negligible. In this case, the boundary conditions were prescribed as

$$\left. \begin{aligned} \text{Case A: } T(0, Y) = T(X, 0) = T(1, Y) = 0, \\ T(X, 1) = 1, \quad \Phi(X, Y) \equiv 0. \end{aligned} \right\} \quad (2.20a)$$

We shall call this case the 'cold wall condition'. The effect of the dissipation term is demonstrated by case B, for which the fixed walls are presumed to be adiabatic, while the temperature of the moving wall is held constant. The temperature is now put in the normalized form $(c_p T/V^2)$, and the boundary conditions are

$$\left. \begin{aligned} \text{Case B: } T(X, 1) = 0, \quad \Phi(X, Y) \neq 0, \\ \left[\frac{\partial T}{\partial X} \right]_{X=0} = \left[\frac{\partial T}{\partial Y} \right]_{Y=0} = \left[\frac{\partial T}{\partial X} \right]_{X=1} = 0. \end{aligned} \right\} \quad (2.20b)$$

This case will be called the 'adiabatic wall condition'. In both cases, the Prandtl number was taken as unity for convenience.

Sample solutions are presented in figure 13 by means of plotted isotherms for $R = 0$, $R = 100$, and $R = 400$. For Stokes flow, the temperature distribution is symmetrical about the vertical centreline of the cavity, in the same way as the flow field. At $T = 400$, the isotherms tend to be convected by the flow, forming a pocket of uniform temperature around the vortex centre. For condition A (cold wall), the value of $\frac{1}{2}$ obtained as the root-mean-square of the surface temperature (analogous to vorticity) agrees very well with that of the inviscid core.

† A similar analysis shows that the temperature is uniform to first order in axisymmetric flow; this is in contrast to the vorticity distribution, which varies linearly with radius.

For condition B (adiabatic wall), the region of nearly uniform temperature is much larger, significant variations occurring only near the downstream corner of the moving wall. It is noteworthy that the bottom and upstream walls have nearly uniform temperature, and that the maximum temperature occurs near the downstream corner of the moving wall.

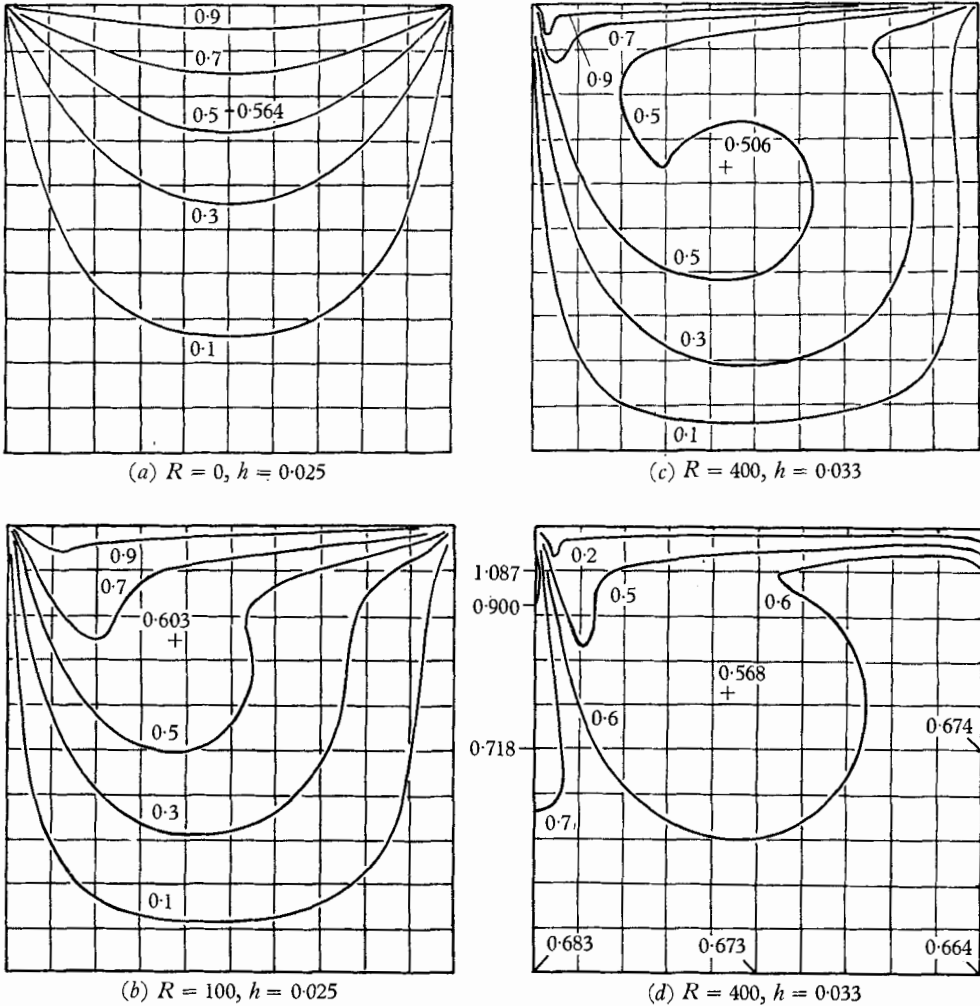


FIGURE 13. Isotherms for viscous eddy in square; (a), (b), (c)—condition A (cold wall); (d)—condition B (adiabatic wall).

The temperature profiles on the vertical line through the vortex centre ($X = 0.567$) are shown in figure 14 for $R = 400$, with both cold and adiabatic wall conditions. The constancy of the temperature in the inviscid core is clearly evident, as well as the thin thermal boundary layer on the moving wall.

The distribution of non-dimensional temperature gradient (heat flux) along the wall is of considerable interest. Figure 15 (a) shows the gradient $\partial T/\partial Y$ on the moving wall for $R = 0, 100$, and 400 for condition A (cold wall). The heat flux is

distributed symmetrically for Stokes flow, but at the higher Reynolds numbers a boundary-layer type of distribution is evident, falling from the singularity at the upstream corner to a minimum value very near the downstream corner. Sufficiently near the corner conduction dominates the heat-transfer mechanism and the asymptotic temperature distribution is $T = 1 - (2\theta/\pi)$, where θ is the

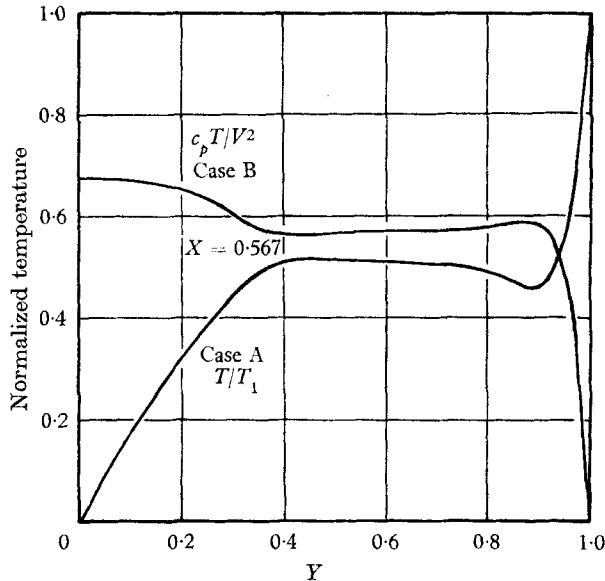


FIGURE 14. Temperature profiles on vertical line through vortex centre.

angle measured from the moving wall. This behaviour is clearly evident in figure 13 for $R = 0$ and $R = 100$. Thus the heat flux is singular like X^{-1} and $(1 - X)^{-1}$. Of course the difference approximation fails near these singularities, but the accuracy of the difference solutions can be assessed by comparing the results for $h = 0.050$ (+) with those for $h = 0.025$ (\times) at $R = 100$. The finer mesh results in higher values of the heat flux near the corners, the coarse-mesh error persisting to about six intervals from the upstream corner. Oscillations of the heat flux can be seen near the downstream corner. These oscillations correspond to the 'troughs' in the isotherms of figure 13, and are caused by convection of the temperature away from the moving wall. Obviously a fine mesh is needed to adequately represent this region. It is interesting to note that at high Reynolds number ($R \geq 400$) the use of a coarse mesh ($h = 0.10$) produced oscillations of the stream function itself; these oscillations of Ψ would be interpreted as discrete eddies, since they form closed streamlines. With the use of a finer mesh these oscillations do not appear, and must be regarded as a property of the difference equations but not of the original Navier-Stokes equations. With regard to the temperature gradient, a pronounced minimum must occur at the trough in the isotherms, and if the oscillations of the difference solution for $R = 400$ are smoothed out, a trend of this type is observed.

In §1 of this study, an analytical expression in closed form, equation (1.21), was obtained for the vorticity at the boundary of a circular eddy in the boundary-

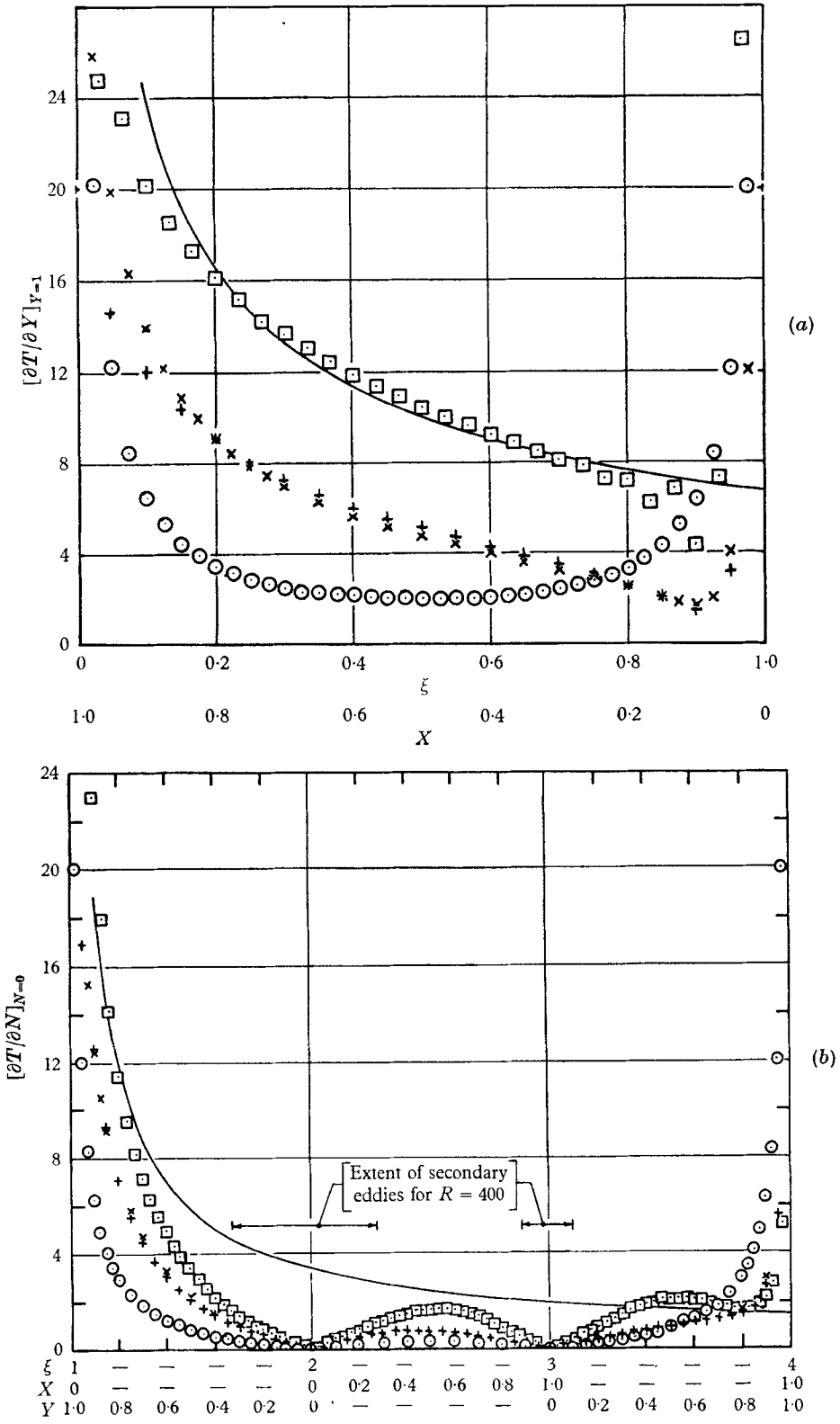


FIGURE 15(a). Normalized heat flux on moving wall. (b) Normalized heat flux on fixed walls. \circ , $R = 0$, $h = 0.025$; $+$, $R = 100$, $h = 0.050$; \times , $R = 100$, $h = 0.025$; \square , $R = 400$, $h = 0.033$; —, equation (2.21).

layer limit. Since temperature and velocity are analogous quantities in the boundary layer for $\sigma = 1$ and $\Phi = 0$, the same expression should provide an approximation to the heat flux in the square for condition A (cold wall). However, to apply this formula, the angular velocity Ω of the basic flow in the circle must be chosen. In the limit $R \rightarrow \infty$, the linearization of § 1 corresponds exactly to an Oseen linearization of the boundary-layer equations. As discussed by Lewis & Carrier (1949), the basic unperturbed flow need not be that outside the boundary layer, but instead should be a suitable average. For the present problem, the basic flow is chosen arbitrarily as $\frac{1}{2}V$; that is, a rough average of the velocity in the boundary layer near the moving wall. This choice is motivated by the fact that the highest heating rates occur in this region, which therefore merits the closest approximation.† With this choice, and in the notation appropriate to the square, the temperature gradient at the wall for case A is obtained from § 1

$$\left[\frac{\partial T}{\partial N} \right]_{N=0} = \left[\frac{\partial}{\partial N} \left(\frac{u}{V} \right) \right]_{N=0} = \sqrt{\frac{R}{8\pi}} [Z(\frac{1}{2}, \xi - \frac{1}{4}) - Z(\frac{1}{2}, \xi)], \quad (2.21)$$

where $R = VL/\nu$, $Z(\frac{1}{2}, \xi)$ is a periodic function which agrees with the generalized Riemann zeta function in its fundamental period $0 < \xi \leq 1$, N is the non-dimensional distance measured inward from the wall ($N = 1 - Y$ on the moving wall), and ξ is the non-dimensional distance measured along the perimeter of the square starting at the upstream corner of the moving wall ($\xi = X/4L$ on the moving wall).

The solid curve in figure 15(a) is a plot of (2.21) for $R = 400$; the agreement with the finite-difference values is excellent, considering the nature of the approximations involved. Equation (2.21) exhibits a singularity $\sim X^{-\frac{1}{2}}$ for $X > 0$ compared with X^{-1} for the full Navier–Stokes equations; consequently it predicts values near the corner higher than the bounded values of the numerical solutions. However, the difference is of the same order as that indicated for different mesh size at $R = 100$. We conclude that (2.21) is at least as accurate as the finite difference results for $R = 400$. Of course equation (2.21), as well as any boundary-layer calculation, will fail to predict the recompression heating at the downstream corner.

The heat flux to the fixed wall is presented in figure 15(b) as $\partial T/\partial N$ vs running length ξ for case A (cold wall) at $R = 0, 100$, and 400. (To interpret the figure, imagine the sides of the square unfolded to lie in the plane of the bottom wall.) The symmetric solution for Stokes flow is evident, with the temperature gradient increasing with increasing Reynolds number, except far downstream where the trend is reversed. This reversal is caused by conduction of heat upstream from the hot moving wall; the region affected by this upstream conduction must shrink with increasing Reynolds number, as indicated by the numerical results. The solid curve in figure 15(b) is equation (2.21) evaluated for $R = 400$. The boundary-layer approximation is inadequate to provide the details of the heating near the bottom of the square, especially near the corners, owing to the low flow velocities

† In another study (Burggraf 1965), the inviscid-core boundary-layer model was applied to open cavities of arbitrary depth. In that case, the emphasis on the moving boundary is even more important since the vorticity of the inviscid core vanishes with increasing depth in a single eddy model.

there. However, it is significant that the heating near the centre of the bottom wall is approaching the boundary-layer value. It is probable that for shallow cavities (compared with the square) the boundary-layer theory would yield satisfactory results for heat transfer to the bottom wall at points sufficiently removed from the corners. For deeper cavities, the growth of the secondary corner eddies would seem to prevent the formation of a true boundary layer anywhere along the bottom wall. On the downstream sidewall $X = 0$, the temperature gradient actually overshoots and then roughly parallels the boundary-layer curve before the ultimate rise near the hot moving wall. The boundary-layer theory would be expected to be valid over much of both sidewalls, and this is verified by the results. It is gratifying that equation (2.21), derived by means of linearized analysis of a circular eddy, provides a satisfactory determination of conditions in the square.

2.9. Related work

Since completing the work described here, the writer has come across several related papers. Professor Van Dyke kindly drew my attention to a Russian paper (Simuni 1964) in which numerical solutions of the Navier–Stokes equations were presented, both for rectangular cavities (the square considered here being a special case) and for channel flow with forward and backward facing steps. The solutions were obtained by considering the large time limit of the unsteady equations of motion; as remarked earlier, this procedure is nearly equivalent to the relaxation procedure used here. Simuni presents ‘solutions’ for Reynolds numbers as high as 1000, showing isolated eddies within the flow. Results of this type were obtained by this author as well, when attempting to carry out calculations at high Reynolds number ($R = 700, 1000$). Since the same type of behaviour could be obtained at lower Reynolds number ($R \leq 400$) by use of a coarse mesh, but not when using a fine mesh, it is this writer’s opinion that Simuni’s anomalous results are properties of the difference equations with coarse mesh but not of the Navier–Stokes equations (Simuni’s minimum mesh size was $\frac{1}{16}$ for $R = 1000$, which the present study has shown to be quite inadequate even at $R = 400$).

Professor Kawaguti has provided this writer with a report on some numerical solutions for the recirculating flow in a square carried out at the University of Wisconsin (Greenspan *et al.* 1964). Solutions were obtained for Reynolds number up to 256 with meshes as small as $\frac{1}{16}$. Because of the coarse mesh, the vortex centre tends erroneously toward the downstream wall, as shown in figure 12. Since Greenspan’s main interest was in the numerical procedure itself, his solutions were presented only as plots of ψ and ω . For the purposes of the present paper, a more detailed analysis was necessary.

An analytical study of the recirculating flow in a square based on Batchelor’s model of an inviscid core matched to a surrounding shear layer has been carried out by Mills (1965). His analysis was much like that of Squire (1956) but based on the Von Mises form of equation. † The results obtained are quite similar to the

† The Von Mises formulation has the virtue of predicting the circulation of the inviscid core as the root-mean-square surface velocity; this result is exact for a circular eddy, and a good approximation for the square, according to the present calculations.

asymptotic limit ($R \rightarrow \infty$) for the circular eddy, discussed earlier. Mills also carried out experiments to verify his analysis. The measured flow properties were in qualitative agreement with the analysis, but the measured vorticity of the inviscid core was about $\frac{1}{3}$ the predicted value. Mills attributes the deviation to the gap between the fixed and moving wall, to the secondary eddies at the bottom of cavity and to three-dimensional effects. Since our numerical solutions show that the vorticity of the inviscid core is given correctly by Batchelor's model, in spite of the presence of secondary eddies, it is concluded that flow through the gaps and the end effects are the main causes of the deviation, especially in view of the singular character of the pressure and shear stress in the corners of the moving wall.

The major part of the research described here was carried out by the author while working at the Lockheed Research Laboratory, Palo Alto, California, with the financial support of the Lockheed Independent Research Program. The author gratefully acknowledges the programming assistance of Mr M. Washington in carrying out §2 of this study.

REFERENCES

- BATCHELOR, G. 1954 *Quart. J. Appl. Math.* **12**, 209.
 BATCHELOR, G. 1956a *J. Fluid Mech.* **1**, 388.
 BATCHELOR, G. 1956b *J. Fluid Mech.* **1**, 177.
 BURGGRAF, O. R. 1965 *Proc. 1965 Heat Transfer and Fluid Mech. Institute*. Stanford University Press.
 CARSLAW, H. S. & JAEGER, J. C. 1959 *Conduction of Heat in Solids* (2nd ed.). Oxford University Press.
 CHAPMAN, D. R., KUEHN, D. M. & LARSON, H. K. 1956 *NACA RM A55L14*.
 COLLATZ, L. 1960 *The Numerical Treatment of Differential Equations* (3rd ed.) Berlin: Springer.
 DEAN, W. R. & MONTAGNON, P. E. 1949 *Proc. Camb. Phil. Soc.* **45**, 389.
 DWIGHT, H. B. 1961 *Tables of Integrals and Other Mathematical Data* (4th ed.). New York: MacMillan.
 FEYNMAN, R. P. & LAGERSTROM, P. A. 1956 IX International Congress of Applied Mechanics, Brussels.
 GIACOMELLI, R. 1934 *Aerodynamic Theory*, Div. D. (ed. Wm. F. Durand). Berlin: Springer.
 GREENSPAN, D., JAIN, P. C., MANOHAR, R., NOBLE, B. & SAKURAI, A. 1964 Numerical studies of the Navier-Stokes equations. *MRC TR* no. 482. Univ. of Wisconsin, May 1964.
 GROVE, A. S. 1963 Ph.D. Thesis, University of California, Berkeley.
 GROVE, A. S., SHAIR, F. H., PETERSEN, E. E. & ACRIVOS, A. 1964 *J. Fluid Mech.* **19**, 60.
 HOERNER, S. 1958 *Fluid Dynamic Drag* (publ. by author). Midland Park, New Jersey, U.S.A.
 HOWARTH, L. 1953 *Modern Developments in Fluid Dynamics: High Speed Flow*. Oxford: Clarendon Press.
 IMAI, I. 1960 *Proc. X Int. Congr. of Appl. Mech.*, Stresa, Italy.
 KAPLUN, S. 1957 *J. Math. & Mech.* **6**, 595.
 KAPLUN, S. & LAGERSTROM, P. 1957 *J. Math. & Mech.* **6**, 585.
 KAWAGUTI, M. 1961 *J. Phys. Soc. Japan*, **16**, 2307.

- LAMB, H. 1932 *Hydrodynamics*, 6th ed. New York: Dover.
- LEWIS, J. A. & CARRIER, G. F. 1949 *Quart. Appl. Math.* **7**, 228.
- LIGHTHILL, M. J. 1962 *Fourier Analysis and Generalized Functions*. Cambridge University Press.
- MILLS, R. D. 1965 *J. Roy. Aero. Soc.* **69**, 116.
- MOFFATT, H. K. 1964 *J. Fluid Mech.* **18**, 1.
- MUSKHELISHVILI, N. I. 1963 *Some Basic Problems of the Mathematical Theory of Elasticity*. Noordhoff, the Netherlands.
- NASH, J. F. 1962 *NPL Aero. Rep.* no. 1006.
- PRANDTL, L. 1934 *Applied Hydro- and Aeromechanics*. New York: McGraw-Hill.
- PROUDMAN, I. & PEARSON, J. R. A. 1957 *J. Fluid Mech.* **2**, 237.
- SIMUNI, L. M. 1964 *Inzhenernii Zhournal*, (USSR), **4**, 446.
- SQUIRE, H. 1956 *J. Roy. Aero. Soc.* **60**, 203.
- TAYLOR, G. I. 1960 *Aeronautics and Astronautics* (eds. N. J. Hoff & W. G. Vincenti). Oxford: Pergamon Press.
- TAYLOR, G. I. 1962 *Miszaklanean der Angewandten Mechanik* (ed. M. Schafer). Berlin: Akademie.
- VAN DYKE, M. D. 1964 *Perturbation Methods in Fluid Mechanics*. New York: Academic Press.
- WHITTAKER, E. T. & WATSON, G. N. 1952. *A Course of Modern Analysis*, 4th ed. Cambridge University Press.